The Relationship between ITCZ Location and Cross-Equatorial Atmospheric Heat Transport: From the Seasonal Cycle to the Last Glacial Maximum

AARON DONOHOE, JOHN MARSHALL, DAVID FERREIRA, AND DAVID MCGEE

Department of Earth and Planetary Sciences, Massachusetts Institute of Technology, Cambridge, Massachusetts

ABSTRACT

The authors quantify the relationship between the location of the intertropical convergence zone (ITCZ) and the atmospheric heat transport across the equator (AHT_{EQ}) in climate models and in observations. The observed zonal mean ITCZ location varies from 5.3°S in the boreal winter to 7.2°N in the boreal summer with an annual mean position of 1.65°N while the AHT_{EQ} varies from 2.1 PW northward in the boreal winter to 2.3 PW southward in the boreal summer with an annual mean of 0.1 PW southward. Seasonal variations in the ITCZ location and AHT_{EQ} are highly anticorrelated in the observations and in a suite of state-of-the-art coupled climate models with regression coefficients of −2.7° and −2.4° PW^{-1} respectively. It is also found that seasonal variations in ITCZ location and AHT_{EQ} are well correlated in a suite of slab ocean aquaplanet simulations with varying ocean mixed layer depths. However, the regression coefficient between ITCZ location and AHT_{EQ} decreases with decreasing mixed layer depth as a consequence of the asymmetry that develops between the winter and summer Hadley cells as the ITCZ moves farther off the equator.

The authors go on to analyze the annual mean change in ITCZ location and AHT_{EQ} in an ensemble of climate perturbation experiments including the response to CO_2 doubling, simulations of the Last Glacial Maximum, and simulations of the mid-Holocene. The shift in the annual average ITCZ location is also strongly anticorrelated with the change in annual mean AHT_{EQ} with a regression coefficient of −3.2° PW^{-1}, similar to that found over the seasonal cycle.

1. Introduction

The atmospheric meridional overturning circulation in the tropics (the Hadley cell; Hadley 1735) controls the spatial distribution of both the tropical precipitation and the meridional heat transport in the atmosphere (AHT); the tropical precipitation maximum—the intertropical convergence zone (ITCZ)—is collocated with the ascending branch of the Hadley cell. The associated meridional AHT is in the direction of motion in the upper branch of the Hadley cell (Held 2001) and therefore is away from the location of ascending motion (see Fig. 1 for a schematic). Provided that the strength of the mass overturning circulation in the Hadley cell increases with meridional distance from the location of ascent, the magnitude of the atmospheric heat transport across

the equator (AHT_{EQ}) is proportional to the location of the ITCZ relative to the equator, with a northern location corresponding to southward atmospheric heat transport across the equator (see Fig. 1). As a consequence, meridional shifts in the ITCZ location are expected to be accompanied by changes in AHT_{EQ} across a myriad of time scales and climate states such as 1) the seasonal cycle, 2) paleoclimate states, 3) idealized climate simulations (Kang et al. 2008), and 4) changes due to increasing greenhouse gas concentrations (Frierson and Hwang 2012). The value of AHT_{EQ}, in turn, is a consequence of the hemispheric difference in energy input to the atmosphere and is influenced by radiation, clouds, aerosols, ocean heat transport, and surface processes at all latitudes (Yoshimori and Broccoli 2008). As a result, forcing and feedbacks in the extratropics can remotely influence the location of the ITCZ (Chiang and Bitz 2005) by way of the mutual connection among the Hadley circulation, AHT_{EQ}, and the ITCZ location.

The relationship between AHT and the ITCZ location was recently demonstrated by Kang et al. (2008) in

Corresponding author address: Aaron Donohoe, Massachusetts Institute of Technology, Department of Earth, Atmospheric and Planetary Sciences, Room 54-918, 77 Massachusetts Avenue, Cambridge, MA 02139-4307.
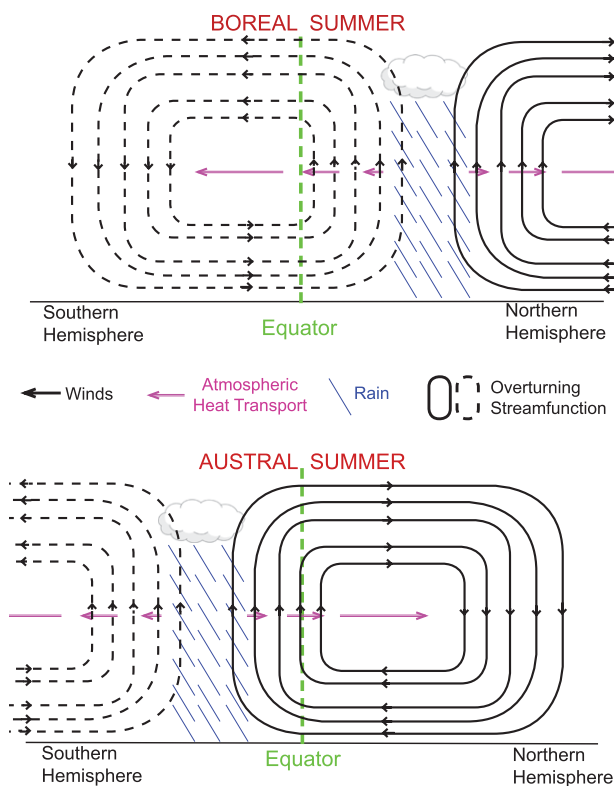E-mail: thedhoe@mit.edu

FIG. 1. Representation of the spatial structure of winds (gray arrows), meridional mass overturning streamfunction (solid and dashed gray contours for the positive and negative streamfunction values, respectively), precipitation (blue lines), and vertically integrated atmospheric heat transport (purple arrows) associated with the Hadley cell for (top) boreal summer and (bottom) austral summer. The equator is the dashed green line.

a slab ocean aquaplanet simulation where a hemispheric asymmetry in atmospheric heating was imposed by introducing a surface heating in the southern extratropics and an equal surface cooling in the northern extratropics. The ITCZ was found to shift toward the heat source and the precipitation maximum was nearly collocated with the location of zero meridional heat transport in the atmosphere, suggesting that a meridional shift of the Hadley cell was the underlying cause of the precipitation shift. Yoshimori and Broccoli (2009, 2008) found that the change in AHT_{EQ} in response to hemispheric asymmetric forcing was closely related to the meridional shift in the Hadley cell, which itself was a response to the hemispheric asymmetry of the forcing and feedbacks. They also noted the concurrent shift in the tropical precipitation along with the Hadley cell but did not quantify the relationship between the change in AHT_{EQ} and the meridional shift of the ITCZ. More recently, Frierson and Hwang (2012) found that the meridional shift in the ITCZ due to increased greenhouse gas concentrations in an ensemble of

simulations was strongly correlated with the change in AHT_{EQ}. They also found that AHT_{EQ} had a large intermodel spread due to differences in extratropical cloud responses. This suggests that the extratropics play an important role in setting the ITCZ location via the interhemispheric asymmetry in energy input to the atmosphere and the associated changes in AHT_{EQ}.

There is widespread paleoclimatic evidence for shifts and/or intensity changes of tropical precipitation in the past including a southward shift of the ITCZ during glacial times (Pahnke et al. 2007), abrupt transitions during glacial times (Wang et al. 2001; Peterson et al. 2000) associated with Dansgaard–Oeschger and Heinrich events, a more northern location during the Holocene thermal maximum (Haug et al. 2001), and a southward shift (estimated to be approximately 5°) during the Little Ice Age (Sachs et al. 2009). Provided the same relationship between the ITCZ and AHT_{EQ} holds across different climate states, each of the ITCZ shifts noted in the paleoclimate records would have an AHT_{EQ} change that can be quantified. Moreover, the change in AHT_{EQ} would have to be associated with a hemispheric asymmetry of atmospheric forcing or climate feedbacks (see Fig. 2). Thus, the quantitative relationship between ITCZ location and AHT_{EQ} provides a framework for comparing precipitation shifts deduced from paleoclimate data and the proposed mechanisms and/or climate forcing that are believed to have caused the precipitation changes (i.e., orbital forcing, changes in land ice and sea ice, cloud albedo changes, a shutdown of the Atlantic meridional overturning circulation, etc.). There is also widespread paleoclimatic evidence for changes in meridional gradients of tropical sea surface temperature (SST) to which the ITCZ is sensitive. Furthermore, SST gradients may be easier to reconstruct from paleoproxies than ITCZ location. Therefore, a quantification of the relationship between SST gradients and ITCZ location is an important task for paleoclimate interpretation.

In this paper, we attempt to quantify the relationship between the location of the ITCZ and AHT_{EQ} in models and observations. We demonstrate that this relationship is robust whether considering the seasonal migration of the ITCZ, the ITCZ shift due to anthropogenic forcing, or the ITCZ shift in past climates including the Last Glacial Maximum. We also study the relationship between tropical SST gradients and the ITCZ location. Our paper is organized as follows. In section 2 we analyze the seasonal cycle of the ITCZ location, AHT_{EQ}, and tropical SST gradients in both the observations (section 2a) and coupled climate models (section 2b). We also analyze the seasonal cycle in an ensemble of slab ocean aquaplanet simulations with ocean varying mixed layer depth (section 2c). In section 3, we focus on the
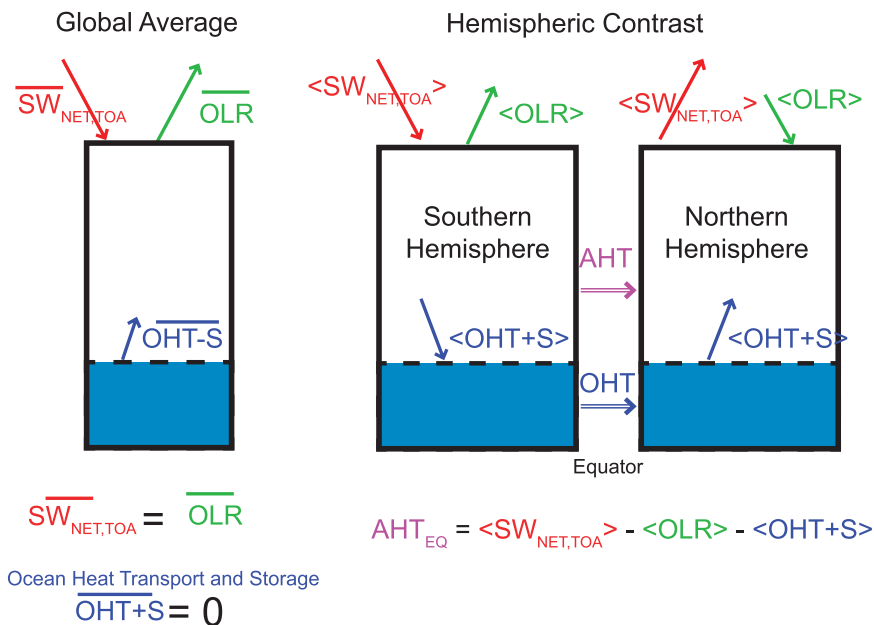
FIG. 2. (left) The global, annual-averaged atmospheric energy budget and (middle), (right) the interhemispheric contrast of the energy budget used to derive the cross-equatorial atmospheric heat transport. The angle brackets indicate the SH integral minus the NH integral divided by 2 and OHT + S is the cross-equatorial ocean heat transport minus storage in each hemisphere.

annual mean shift in the ITCZ, AHT_{EQ}, and tropical SST gradients in model simulations of CO_2 doubling, the Last Glacial Maximum, and 6000 years before present. We conclude with a summary and discussion in section 4.

2. Seasonal cycle of atmospheric heat transport and tropical precipitation

In this section, we analyze the relationship between ITCZ location and AHT_{EQ} over the seasonal cycle. In the boreal summer, the Northern Hemisphere (NH) receives excess insolation relative to the annual mean, leading to atmospheric heating (Donohoe and Battisti 2013). In contrast, the Southern Hemisphere (SH) receives a deficit of insolation relative to the annual mean, leading to atmospheric cooling. The hemispheric asymmetry of atmospheric energy input is largely balanced by atmospheric energy transport from the source of atmospheric heating to the cooling, resulting in southward atmospheric heat transport across the equator (Fasullo and Trenberth 2008). The Hadley cell and ITCZ shift northward toward the warmer SSTs, which positions the southern branch of the Hadley cell over the equator, resulting in southward AHT_{EQ} in the thermally direct Hadley cell. Similarly, in the austral summer, AHT_{EQ} is

northward and the ITCZ is in the Southern Hemisphere. We analyze the seasonal cycle of the observations in section 2a, coupled models in section 2b, and slab ocean aquaplanet simulations with varying mixed layer depths in section 2c.

a. Observations

1) DATA SOURCES AND METHODS

Here we describe the data sources and calculation methods for analyzing the relationship among the ITCZ location, the tropical SST gradient, and AHT_{EQ} in the observations.

(i) Tropical precipitation and ITCZ location

We use the precipitation climatology from the National Oceanographic and Atmospheric Administration (NOAA) Climate Prediction Center (CPC) merged analysis (Xie and Arkin 1996), a gridded data product that combines gauge measurements, satellite observations, and numerical models. The climatology is composed of data from 1981 to 2010. We use the precipitation centroid (P_{CENT}) defined by Frierson and Hwang (2012) as a metric for the location of the ITCZ–tropical precipitation maximum. There, the precipitation centroid was defined as the median of the zonal average precipitation from 20°S to 20°N. The precipitation is interpolated to a 0.1° grid over

the tropics to allow the precipitation centroid to vary at increments smaller than the grid spacing.

(ii) Tropical SST gradient

We use the Extended Reconstructed Sea Surface Temperature (ERSST) data from Reynolds and Smith (1994), version 3b (Smith et al. 2008), which takes ship and buoy measurements and produces a gridded dataset at 2° resolution using an optimum interpolation method. We use the climatological data calculated between 1981 and 2010. As a metric for the interhemispheric difference of tropical SST, we calculate ΔSST as the spatially weighted SST between the equator and 20°N minus the spatially weighted SST between the equator and 20°S.[1]

(iii) Atmospheric heat transport across the equator

The atmospheric heat transport is derived from the National Centers for Environmental Prediction (NCEP) four-times-daily reanalysis fields (Kalnay et al. 1996) with a (horizontal) spectral resolution of T62 and 17 vertical levels. The atmospheric heat transport is calculated by first balancing the atmospheric mass budget in the reanalysis data with a barotropic wind correction as in Trenberth (1997) and subsequently calculating the meridional flux of moist static energy[2] and vertically integrating. This procedure is used to compose monthly averaged atmospheric heat transport from 1981 to 2010 and the climatological average over this period is used in this study.

We now derive an expression for AHT_{EQ} in terms of the hemispheric contrast of net energy (radiative and turbulent) input into the atmosphere (see Fig. 2) starting from the energy budget of the climate system at each latitude:

$$\text{SW}_{\text{NET,TOA}} - \text{OLR} = \frac{d}{dt}\left[\frac{1}{g}\int_0^{P_s}(c_p T + Lq)\,dP\right]$$
$$+ \nabla \cdot (\text{OHT} + \text{AHT}) + \text{OHS}, \tag{1}$$

where $\text{SW}_{\text{NET,TOA}}$ is the net downwelling shortwave flux at the top of the atmosphere (TOA), OLR is the outgoing longwave radiation at the TOA, T is temperature, c_p is the heat capacity at constant pressure, L is the latent heat of vaporization of water, q is the specific humidity, P_S is the surface pressure, and OHS is the

ocean heat storage. And, $\nabla \cdot (\text{OHT} + \text{AHT})$ is the divergence of the ocean and atmospheric heat transport, respectively. The global average (denoted by overbars) atmospheric energy budget for each month satisfies the equation

$$\overline{\text{SW}_{\text{NET,TOA}}} - \overline{\text{OLR}} = \frac{d}{dt}\left[\overline{\frac{1}{g}\int_0^{P_s}(c_p T + Lq)\,dP}\right] + \overline{\text{OHS}}, \tag{2}$$

where the ocean and atmospheric energy flux divergences disappear in the global average. The left-hand side of the equation represents the net radiative heating of the climate system and the right-hand side represents energy storage in the atmosphere (we will hereafter denote this term as $\text{STOR}_{\text{atmos}}$) and ocean respectively. If we subtract Eq. (2) from Eq. (1) and spatially integrate over each hemisphere separately, we can derive an expression for AHT_{EQ} by noting that the heat transport divergence averaged over the Southern Hemisphere equals the heat transport across the equator:

$$\text{AHT}_{\text{EQ}} = \langle \text{SW}_{\text{NET,TOA}} \rangle - \langle \text{OLR} \rangle - \langle \text{OHT} + S \rangle$$
$$- \langle \text{STOR}_{\text{atmos}} \rangle, \tag{3}$$

where brackets indicate the spatial integral of the anomaly from the global averaged over the Southern Hemisphere (or, equivalently, the negative of the spatial integral over the Northern Hemisphere) and $\langle \text{OHT} + S \rangle$ is the combined effect of cross-equatorial ocean heat transport and ocean heat storage in each hemisphere ($\langle \text{OHT} + S \rangle$ is positive for northward oceanic heat transport at the equator and/or more heat storage in the Southern Hemisphere). A schematic of the interhemispheric energy budget cast in these terms is shown in Fig. 2. In the annual average, both $\langle \text{STOR}_{\text{atmos}} \rangle$ and ocean heat storage are zero if the system is in equilibrium and Eq. (4) simplifies to

$$\text{AHT}_{\text{EQ}} = \langle \text{SW}_{\text{NET,TOA}} \rangle - \langle \text{OLR} \rangle - \text{OHT}_{\text{EQ}}. \tag{4}$$

As discussed in Fasullo and Trenberth (2008), the predominant seasonal energy balance is between $\text{SW}_{\text{NET,TOA}}$ and ocean heat storage and this near balance leads to compensating energy fluxes at the TOA and surface. We therefore follow the methodology of Donohoe and Battisti (2013) and divide the atmospheric heating into a component due to shortwave absorption in the atmospheric column (SWABS) and the upward flux of turbulent and longwave radiation from the surface to the atmosphere (SHF). Equation (4) becomes

---

[1] Similar results are found using the regions equatorward of 15° and 30° in each hemisphere.

[2] Moist static energy is the sum of sensible, latent, and potential energy ($c_p T + Lq + gZ$).

$$\mathrm{AHT_{EQ}} = \langle \mathrm{SWABS} \rangle - \langle \mathrm{OLR} \rangle + \langle \mathrm{SHF} \rangle - \langle \mathrm{STOR_{atmos}} \rangle, \tag{5}$$

where SWABS is the shortwave radiation absorbed in the atmosphere,

$$\mathrm{SWABS} = \mathrm{SW}{\downarrow}_{\mathrm{TOA}} - \mathrm{SW}{\uparrow}_{\mathrm{TOA}} + \mathrm{SW}{\uparrow}_{\mathrm{SURF}} \\ - \mathrm{SW}{\downarrow}_{\mathrm{SURF}}, \tag{6}$$

and represents the sun directly heating the atmosphere. Here SHF is energy fluxed from the surface to the atmosphere and is the sum of sensible heat fluxes (SENS), latent heat fluxes (LH), and longwave fluxes (LW) from the surface into the atmosphere:

$$\mathrm{SHF} = \mathrm{SENS}{\uparrow}_{\mathrm{SURF}} + \mathrm{LH}{\uparrow}_{\mathrm{SURF}} + \mathrm{LW}{\uparrow}_{\mathrm{SURF}} \\ - \mathrm{LW}{\downarrow}_{\mathrm{SURF}}. \tag{7}$$

We note that Eq. (5) is merely a regrouping of the shortwave flux terms in Eq. (4).[3]

We use longwave and shortwave radiative fluxes from the Clouds and Earth's Radiant Energy System (CERES) experiment (Wielicki et al. 1996) to calculate $\langle \mathrm{SWABS} \rangle$ and $\langle \mathrm{OLR} \rangle$. All calculations are performed separately for each of the four CERES instruments (FM1 and FM2 on *Terra* from 2000 to 2005 and FM3 and FM4 on *Aqua* from 2002 to 2005). We then average the results over the four instruments. The quantity $\langle \mathrm{STOR_{atmos}} \rangle$ is calculated as the finite difference of the vertically integrated temperature and specific humidity from the NCEP reanalysis climatology. As in Donohoe and Battisti (2013), $\langle \mathrm{SHF} \rangle$ is calculated as the residual of radiative heating, atmospheric storage, and the atmospheric heat transport divergence (from NCEP reanalysis).

The seasonal amplitude and phase used in our analysis are defined as the amplitude and phase of the annual harmonic.

2) RESULTS

A scatterplot of the monthly average P_{CENT} versus $\mathrm{AHT_{EQ}}$ and $\Delta \mathrm{SST}$ is shown in Fig. 3. The precipitation centroid varies from 5.3°S in February to 7.2°N in August and has an annual average of 1.65°N. This seasonal cycle of ITCZ location is slightly damped (equatorward) of other common metrics of ITCZ location (e.g., the latitude of maximum zonal mean precipitation, Xian and Miller 2008). It can be seen that P_{CENT} spends four months of the year in the Southern Hemisphere during the austral

---

[3] In this framework, the net flux into the ocean is $\mathrm{SW_{NET,SURF}} - \mathrm{SHF} = \mathrm{OHT} + S$.
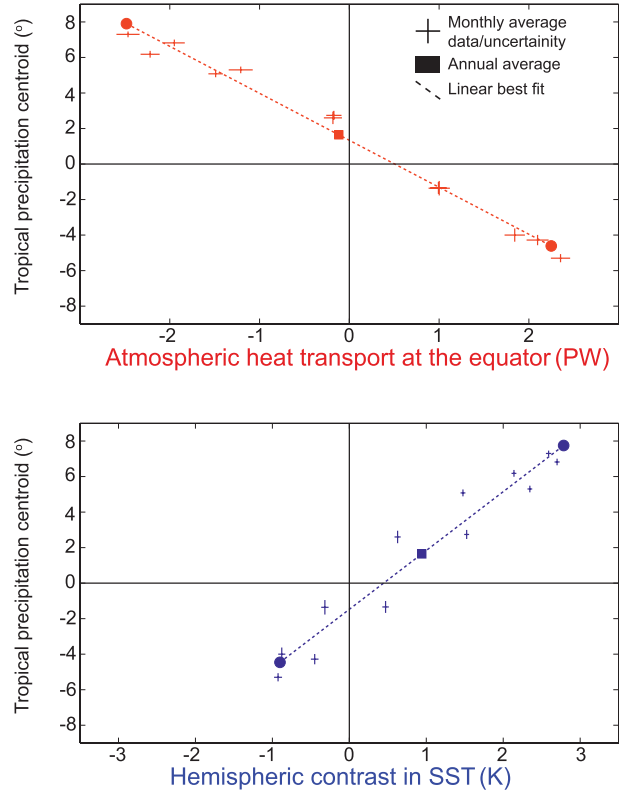

FIG. 3. (top) Scatterplot of the seasonal cycle of tropical precipitation centroid vs cross-equatorial atmospheric heat transport. Each cross is centered on the monthly average and the length of the cross on each axis represents the 95% confidence interval assessed from the interannual variability. The filled box is the annual average. The dashed line is the linear best fit to the monthly averages. (bottom) As at top, but for the tropical precipitation centroid vs the interhemispheric difference in tropical SST.

summer as the most intense precipitation is found in the South Pacific convergence zone at this time of year (not shown) and the zonal mean precipitation maximum moves to southern latitudes. We note that although the marine ITCZ defined in the eastern Pacific and Atlantic by Waliser and Gautier (1993) never moves south of the equator, the global ITCZ defined in the same study does move into the Southern Hemisphere and agrees very well with our precipitation centroid.

The value of $\mathrm{AHT_{EQ}}$ varies from 2.1 PW northward in February to 2.3 PW southward in August with an annual average of 0.1 PW southward. The vast majority (over 99%) of the seasonal variations in cross-equatorial atmospheric heat transport are associated with the zonal and time averaged meridional overturning circulation at the equator (i.e., the Hadley cell), which reverses seasonally (Dima and Wallace 2003). The seasonal variations in cross-equatorial heat transport associated with the stationary and transient eddies are two orders of magnitude smaller in magnitude (not shown). The

hemispheric contrast of tropical SST, ΔSST, has a maximum value of 2.7 K in September and a minimum of -0.9 K in March; it lags the insolation by approximately 3 months and lags both P_{CENT} and AHT_{EQ} by approximately one month. The annual average ΔSST value is 0.9 K, which corresponds with the maximum tropical SSTs being located north of the equator in the annual average.

The seasonal variations in P_{CENT} and AHT_{EQ} are strongly anticorrelated (as anticipated from Fig. 1) with an R^2 value of 0.99 and a slope of $-2.7 \pm 0.6°$ PW^{-1}. This result suggests that seasonal migrations in both P_{CENT} and AHT_{EQ} primarily reflect the seasonal migration of the Hadley cell. This interpretation is also supported by analysis of the seasonal migration of the overturning streamfunction and the partitioning of AHT_{EQ} into latent, sensible, and potential components (not shown); the total AHT_{EQ} is always of the same sign as the potential energy heat transport and is opposed by the sensible and latent heat transport as would be expected from a thermally direct circulation in a stably stratified column with moisture and temperature decreasing with height. The linear best fit in Fig. 3 passes close to but not through the origin with a y intercept of 1.2°N. This offset is not anticipated from our idealized model presented in the introduction and suggests that, although the vast majority of seasonal variations in P_{CENT} and AHT_{EQ} are explained by meridional shifts in the Hadley cell, other phenomena influence either the precipitation and/or atmospheric heat transport. We speculate that monsoonal circulations that are related to zonal inhomogeneities in coastlines and atmospheric circulations—and are thus poorly captured by our zonal average analysis—may bias the precipitation centroid farther north than what would be defined from the Hadley cell–related precipitation only.

Seasonal variations in P_{CENT} and ΔSST are strongly correlated (note that the green ΔSST x axis in Fig. 3 has been inverted) with an R^2 value of 0.94 and a slope of 3.3° K^{-1}. The seasonal correlation between P_{CENT} and ΔSST is slightly smaller than that between P_{CENT} and AHT_{EQ} because ΔSST lags the other two variables by approximately 1 month, leading to an elliptical pattern in the ΔSST (green crosses) scatterplot whereas the AHT_{EQ} (red crosses) scatterplot falls nearly on the linear best fit. The y intercept of the linear best fit between P_{CENT} and ΔSST is $-1.4°$ and is not anticipated a priori. Rather, one might suppose that, if SST determined ITCZ location, a SST distribution that is symmetric about the equator (ΔSST $= 0$) would lead to an ITCZ on the equator ($P_{CENT} = 0$). Instead, the observations suggest that the ITCZ is located south of the equator when there is no interhemispheric contrast of tropical SSTs. The cause of

this offset from the origin in the observations is unclear to us.

Seasonal variations in AHT_{EQ} are driven by hemispheric asymmetries in energy input into the atmosphere and can be diagnosed from Eqs. (4) and (5). Ultimately, seasonal variations in AHT_{EQ} result from the seasonal migration of the insolation maximum between the hemispheres although the vast majority of the seasonal variations in insolation are stored in the ocean (Fasullo and Trenberth 2008); the hemispheric asymmetry of net shortwave flux at the TOA [$\langle SW_{NET,TOA} \rangle$ in Eq. (4)] has a seasonal amplitude of 22.4 PW and is primarily (83%) balanced by the hemispheric asymmetry of ocean heat storage ($\langle OHT + S \rangle$) with a seasonal magnitude of 18.5 PW out of phase with insolation. Therefore, we chose to recast the interhemispheric contrast of the atmospheric energy budget in terms of the absorption of shortwave radiation in the atmosphere ($\langle SWABS \rangle$) and the nonsolar exchange of energy between the surface and the atmosphere ($\langle SHF \rangle$) as expressed in Eq. (5) (Donohoe and Battisti 2013). The seasonal cycle of the interhemispheric contrast in the atmospheric energy fluxes is shown in Fig. 4.

The summer hemisphere absorbs more shortwave radiation in the atmospheric column than the winter hemisphere and, in the absence of compensating energy fluxes, would result in a 7.1-PW seasonal amplitude of AHT_{EQ} with northward heat transport peaking near (5 days after) the austral summer solstice. However, 46% of this interhemispheric energy contrast is balanced by air–surface energy exchange ($\langle SHF \rangle$) with the atmosphere warming the ocean in the summer hemisphere and the ocean heating the atmosphere in the winter hemisphere. Additionally, 16% of the seasonal variations in $\langle SWABS \rangle$ is radiated to space as an interhemispheric contrast in OLR ($\langle OLR \rangle$). Both $\langle SHF \rangle$ and $\langle OLR \rangle$ are nearly antiphased with the insolation and $\langle SWABS \rangle$ (with a phase lead of 1 day and phase lag of 12 days, respectively). The interhemispheric contrast of atmospheric energy storage ($\langle STOR_{ATMOS} \rangle$) has a seasonal amplitude of 2.3 PW and is associated with the heating (in the extratropics) and moistening (in the tropics) of the atmospheric column in the summer hemisphere and the cooling and drying of the column in the winter hemisphere. It leads the insolation by approximately 60 days, which is expected from a system where the negative feedbacks (OLR and atmospheric heat transport) are substantially stronger than the thermal inertia (Donohoe and Battisti 2012). As a consequence, the sum of all the other energy fluxes, which is equal to AHT_{EQ} by Eq. (5), is substantially smaller than $\langle SWABS \rangle$ (due to the damping by $\langle SHF \rangle$ and $\langle OLR \rangle$) and lags the insolation (due to the phase lead of atmospheric energy
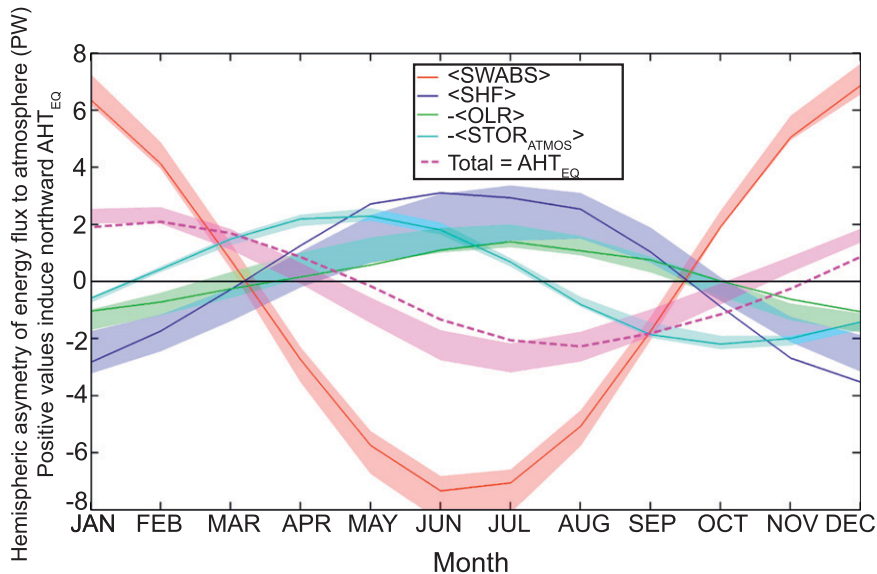
FIG. 4. Seasonal cycle of hemispheric contrast in energy fluxes defined as half the difference in spatial integral of fluxes in the SH minus that in the NH. The solid lines are the observations and the shaded region represents ± 1 standard deviation about the CMIP3 PI ensemble average. The terms are defined in the legend and discussed in the text in reference to Eq. (5). The first four terms in the legend sum to yield AHT_{EQ}.

storage, $\langle STOR_{ATMOS} \rangle$); AHT_{EQ} has a seasonal amplitude of 2.2 PW and lags the insolation by 46 days.

3) THE QUANTITATIVE RELATIONSHIP BETWEEN ITCZ LOCATION AND ATMOSPHERIC HEAT TRANSPORT ACROSS THE EQUATOR

Figure 3 suggests that the ITCZ location (P_{CENT}) covaries with the atmospheric heat transport across the equator (AHT_{EQ}) with a 1-PW change in AHT_{EQ} corresponding to a $2.7°$ meridional shift in the ITCZ location. To put this quantitative relationship in perspective, we remind the reader that the observed annual mean AHT_{EQ} is -0.1 PW and that the maximum value of AHT at all latitudes is on the order of 5 PW (Trenberth and Caron 2001). This quantitative relationship suggests that modest shifts in tropical precipitation must be accompanied by fairly substantial perturbations to the interhemispheric energy budget (Fig. 2), the focus of this manuscript. We now ask this question: What physical processes set the quantitative relationship between P_{CENT} and AHT_{EQ}?

If the atmospheric heat transport in the tropics is dominated by the Hadley cell, then AHT_{EQ} is proportional to the mass overturning streamfunction (Ψ) at the equator—defined as positive when the motion in the upper branch is northward—times the average energy contrast between the poleward and equatorward flow (ΔT_E; see Czaja and Marshall 2006):

$$AHT_{EQ} \approx \Psi_{EQ} c_p \Delta T_E. \tag{8}$$

Indeed, the monthly average overturning streamfunction at 500 hPa over the equator is highly correlated ($R^2 = 0.99$) with AHT_{EQ} with a regression coefficient of 0.014 PW Sv^{-1} (top panel of Fig. 5). The regression coefficient corresponds to an equivalent potential temperature contrast between the poleward and equatorward moving air ΔT_E of 14 K and is consistent with a meridional overturning circulation that is on the order of 600 hPa deep given the average vertical profile of temperature and moisture in the tropics. This result suggests that seasonal variations of Ψ_{EQ} control AHT_{EQ} while ΔT_E remains fairly constant. If ΔT_E is constant, then we can derive a relationship between the latitude of zero mass overturning ($\theta_{\Psi=0}$) and the AHT_{EQ} by use of a Taylor expansion of the overturning streamfunction about its zero crossing and Eq. (8):

$$AHT_{EQ} \approx -\theta_{\Psi=0} \left. \frac{\partial \Psi}{\partial \theta} \right|_{\theta_{\Psi=0}} c_p \Delta T_E. \tag{9}$$

The expected relationship between $\theta_{\Psi=0}$ and AHT_{EQ} from Eq. (9) [using ΔT_E of 14 K and the climatological mean of $\partial \Psi / \partial \theta |_{\theta_{\Psi=0}}$ of 8 Sv ($°$)$^{-1}$; here 1 Sv is defined as 1×10^9 kg s^{-1} as in Czaja and Marshall (2006)] is shown by the black dashed line in the bottom panel of Fig. 5: it has a slope of $-8.9°$ PW^{-1}. This expectation compares
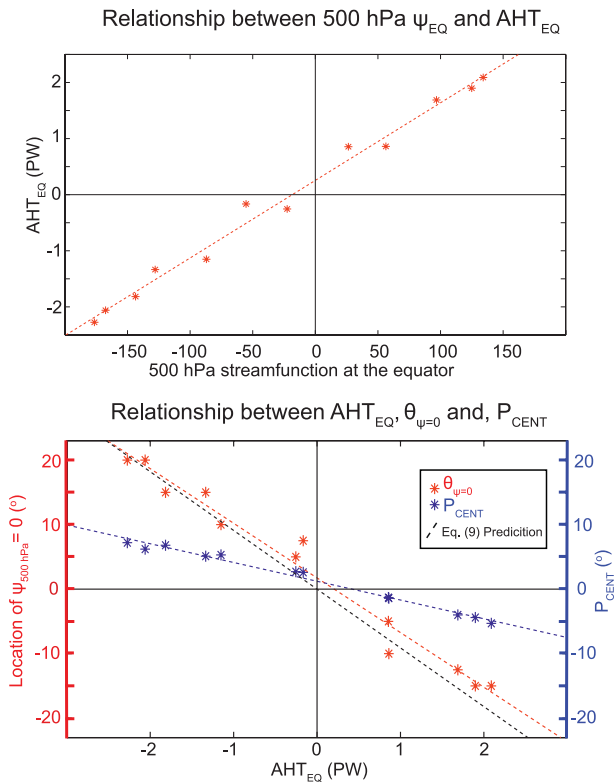
Relationship between 500 hPa ψ$_{EQ}$ and AHT$_{EQ}$

Relationship between AHT$_{EQ}$, θ$_{ψ=0}$, and P$_{CENT}$

FIG. 5. (top) Scatterplot of AHT$_{EQ}$ vs the mass overturning streamfunction at 500 hPa over the equator over the seasonal cycle in the observations. Each asterisk is a monthly average and the dashed line is the linear best fit. (bottom) Scatterplot of the location of the 0 mass overturning streamfunction $\theta_{\Psi=0}$ at 500 hPa vs AHT$_{EQ}$ (red asterisk and linear best fit dashed line) and P$_{CENT}$ vs AHT$_{EQ}$ (blue asterisk and linear best fit dashed line). The expected relationship between $\theta_{\Psi=0}$ and AHT$_{EQ}$ from Eq. (9) is shown by the dashed black line.

well with the monthly average values of $\theta_{\Psi=0}$ and AHT$_{EQ}$ (red asterisks in the lower panel Fig. 5), suggesting that $\partial\Psi/\partial\theta$ is fairly spatially uniform in the tropics. Equation (9) is useful because, if the maximum ascent and precipitation occurs where the mass overturning streamfunction changes sign ($\theta_{\Psi=0}$), then we would expect P$_{CENT}$ and AHT$_{EQ}$ to follow the same relationship as that found between $\theta_{\Psi=0}$ and AHT$_{EQ}$ (i.e., approximately $-8.9°$ PW^{-1}). However, the slope between P$_{CENT}$ and AHT$_{EQ}$ is substantially smaller ($-2.7°$ PW^{-1}; blue asterisks in the lower panel of Fig. 5), suggesting that P$_{CENT}$ remains substantially equatorward of the zero streamfunction as the Hadley cell seasonally moves off the equator. Lindzen and Hou (1988) previously found that the maximum upward ascent occurs equatorward of the location of zero streamfunction in an idealized model of the Hadley circulation; we will return to a discussion of this point in section 2c(2).

b. Coupled climate models

1) MODEL RUNS USED AND METHODOLOGY

We use model output from phase 3 of the Coupled Model Intercomparison Project (CMIP3) multimodel database (Meehl et al. 2007): an ensemble of standardized coupled climate simulations from 25 different climate models that were used in the Intergovernmental Panel on Climate Change's Fourth Assessment Report. We analyze the preindustrial (PI) simulations here. In those simulations, greenhouse gas concentrations, aerosols, and solar forcing are fixed at preindustrial levels and the models are run for 400 years. The last 20 years of the PI simulations are used to calculate climatological fields. The 16 models used in this study are listed in Table 1.

The turbulent and radiative energy fluxes at the surface and TOA are provided as model output fields. This allows $\langle$SWABS$\rangle$ and $\langle$SHF$\rangle$ to be directly calculated from Eqs. (6) and (7). The $\langle$OLR$\rangle$ is directly calculated and $\langle$STOR$_{ATMOS}\rangle$ is calculated from finite difference of the monthly averaged vertically integrated temperature and specific humidity fields; AHT$_{EQ}$ is then calculated from the residual of the other terms in Eq. (5).

2) RESULTS

We show the seasonal amplitude (given by half the length of the line) and the regression coefficient (given by the slope of the line) between P$_{CENT}$ and AHT$_{EQ}$ for each CMIP3 ensemble member in the upper panel of Fig. 6. We define the seasonal amplitude of P$_{CENT}$ and AHT$_{EQ}$ as the amplitude of the annual harmonic of each variable. The CMIP3 ensemble mean regression coefficient between P$_{CENT}$ and AHT$_{EQ}$ is $-2.4° \pm 0.4°$ PW^{-1} (the slope of the thick black line) and is slightly smaller but statistically indistinguishable from the value of $-2.7° \pm 0.6°$ PW^{-1} found in the observations (the thick purple line). Table 2 lists the seasonal statistics of P$_{CENT}$ and AHT$_{EQ}$ in observations and the models. Seasonal variations in P$_{CENT}$ and AHT$_{EQ}$ are significantly correlated with each other in all models with an ensemble average correlation coefficient of -0.89. On average, the linear best fits in the models come closer to the origin than do the observations (thick black line in Fig. 6), conforming to our idealized expectation that when the precipitation is centered on the equator, the ascending branch of the Hadley cell will also be on the equator, resulting in zero cross-equatorial heat transport in the atmosphere. The relationship between P$_{CENT}$ and AHT$_{EQ}$ over the seasonal cycle is fairly consistent from one model to the next (all the slopes in Fig. 6 are similar) and is similar to the relationship found in the observations. This suggests that fairly robust physics underlie the relationship between P$_{CENT}$ and AHT$_{EQ}$, mainly the

TABLE 1. Models used in this study and their resolution. The horizontal resolution refers to the latitudinal and longitudinal grid spacing or the spectral truncation. The vertical resolution is the number of vertical levels.

Abbreviation	Full name	Horizontal resolution	Vertical resolution
BCCR-BCM2.0	Bjerknes Centre for Climate Research (University of Bergen, Norway) Bergen Climate Model, version 2	T63	L31
CCCMA-CGCM3.1	Canadian Centre for Climate Modeling and Analysis (Canada) Coupled General Circulation Model, version 3.1	T47	L31
CNRM-CM3	Centre National de Recherches Météorologiques (France) Coupled Global Climate Model, version 3	T63	L45
CSIRO-Mk3.0	Commonwealth Scientific and Research Organization (Australia) Mark 3.0	T63	L18
GFDL-CM2.0	Geophysical Fluid Dynamics Laboratory (United States) Climate Model, version 2.0	$2.0° \times 2.5°$	L24
GFDL-CM2.1	GFDL (United States) Climate Model, version 2.1	$2.0° \times 2.5°$	L24
IAP-FGOALS	Institute of Atmospheric Physics [National Key Laboratory of Numerical Modeling for Atmospheric Sciences and Geophysical Fluid Dynamics (LASG), China] Flexible Global Ocean–Atmosphere–Land System Model	T42	L26
MPI-ECHAM5	Max Planck Institute for Meteorology (Germany) ECHAM	T63	L31
INM-CM3.0	Institute for Numerical Mathematics (Russia) Coupled Model, version 3.0	$4° \times 5°$	L21
IPSL-CM4.0	L'Institute Pierre Simon Laplace (France) Coupled Model, version 4	$2.5° \times 3.75°$	L19
MIROC3.2(medres)	National Institute for Environmental Studies (NIES) and Frontier Research Center for Global Change (FRCGC; Japan) Model for Interdisciplinary Research on Climate (MIROC) 3.2, medium-resolution version	T42	L20
MIROC3.2(hires)	NIES and FRCGC (Japan) MIROC 3.2, high-resolution version	T106	L56
MRI-CGCM2.3.2a	Meteorological Research Institute (Japan) Coupled General Circulation Model, version 2.3.2a	T42	L30
NCAR-CCSM3.0	National Center for Atmospheric Research (United States) Community Climate System Model, version 3.0	T85	L26
UKMO-HadCM3	Hadley Centre for Climate Prediction and Research (United Kingdom), third climate configuration of the Met Office Unified Model	$2.5° \times 3.8°$	L19
MIUB-ECHOg	Meteorological Institute of the University of Bonn (Germany) ECHAM and the global Hamburg Ocean Primitive Equation	T30	L19

mutual relationship among the tropical precipitation maximum, AHT_{EQ}, and the location of the Hadley cell. The precipitation centroid lags the cross-equatorial atmospheric heat transport in the models by 29 days in the ensemble average (with a standard deviation of 6 days). This is in contrast to the observations where there is virtually no (<2 days) phase shift between P_{CENT} and AHT_{EQ}. We further discuss this result later in this section.

We note that the intermodel spread of the annual mean P_{CENT} and AHT_{EQ} are significantly correlated with each other with a regression coefficient of −0.79 and a slope that is statistically indistinguishable from the ensemble mean seasonal relationship between P_{CENT} and AHT_{EQ}. This result suggests that the same physics that determine the seasonal migration of the ITCZ location and AHT_{EQ} (associated with meridional shifts in the Hadley cell) also govern the intermodel spread of ITCZ location in the annual mean. Although there are

slight variations in the relationship between P_{CENT} and AHT_{EQ} between the different models and the observations, the robust relationship between P_{CENT} and AHT_{EQ} allows one to predict P_{CENT} from AHT_{EQ} (or vice versa) with the same relationship holding for the seasonal problem and for the annual mean intermodel spread problem.

Histograms of the monthly mean P_{CENT} over the last 150 years of the simulations are shown in Fig. 7. The P_{CENT} distribution in each model is bimodal; P_{CENT} is most often found in one of the two solstitial extremes (Lindzen and Hou 1988) and is rarely found in the vicinity of the annual average. By construction, the annual average is the average of the northernmost and southernmost extent shown by the shaded dots in Fig. 7 (and defined as the annual mean plus or minus the seasonal amplitude). Therefore, in order to shift the annual average P_{CENT} northward, the ITCZ must either migrate farther into (or stay longer in) the Northern Hemisphere in the boreal

TABLE 2. Seasonal amplitude (amplitude of the annual harmonic) and regression coefficients of precipitation centroid, AHT_{EQ}, and ΔSST in the observations and in CMIP3 preindustrial models. The 95% confidence limits are listed after each value and are assessed from the interannual spread in the observations, intermodel spread in the models, and uncertainty in the regression coefficients.

	Observations	CMIP3 ensemble mean
Centroid seasonal amplitude (°)	6.3 ± 0.2	6.6 ± 0.8
AHT_{EQ} seasonal amplitude (PW)	2.2 ± 0.1	2.5 ± 0.3
ΔSST	1.8 ± 0.1	2.0 ± 0.3
P_{CENT} vs AHT_{EQ} regression coef (° PW^{-1})	−2.7 ± 0.6	−2.4 ± 0.4
P_{CENT} vs ΔSST regression coef (° K^{-1})	3.3 ± 0.6	3.7 ± 0.7

summer or migrate less far into (or spend less time in) the Southern Hemisphere during the austral summer. The models with an anomalous (relative to the ensemble average) northward annual mean P_{CENT} (the models shown in red toward the top of the figure) tend to have a P_{CENT} that migrates farther north in the boreal summer. In contrast, the models with a southward annual mean P_{CENT} (the models shown in blue toward the bottom of the figure) tend to have a P_{CENT} that migrates less far north in the boreal summer. Similarly, the magnitude of the southward migration of the ITCZ during the austral winter is largest in the models with an annual mean ITCZ location south of the ensemble average (blue dots) and smallest in the models with an annual mean ITCZ location north of the ensemble mean (red dots). We further discuss the relationship between the seasonal extremes and the annual mean of P_{CENT} and AHT_{EQ} in section 4.

The seasonal amplitude of AHT_{EQ} is 2.5 ± 0.3 PW in the models and is larger but within the error bars of that found in the observations (2.2 PW; Table 2). As a consequence, the seasonal amplitude in P_{CENT} of 6.6° ± 0.8° is also larger than that in the observations (6.3°). The amplitude and phasing of $\langle SWABS \rangle$, $\langle OLR \rangle$, and $\langle STOR_{ATMOS} \rangle$ closely match those found in the observations (cf. the shaded regions and the solid lines in Fig. 4). In contrast, $\langle SHF \rangle$ in the models lags $\langle SHF \rangle$ in the observations by 16 days on average. As a result, the net hemispheric contrast in energy input to the atmospheric column is more in phase with the insolation in the models than in the observations and AHT_{EQ} lags the insolation by 25 days in the models as compared to 46 days in the observations. This offers a partial explanation for why the seasonal migration of P_{CENT} lags that in AHT_{EQ} in the models (by 29 days) but not in the observations. However, the root cause of this discrepancy and its relationship to the seasonal migration of the Hadley circulation is unclear to us.

The seasonal amplitude and the regression coefficient (given by the slope of the line) between P_{CENT} and ΔSST for each CMIP3 ensemble member is shown in the lower panel of Fig. 6 along with the observations. The ensemble average of the seasonal amplitude of ΔSST is 2.0 ± 0.3 K and compares well with that in the observations (1.8 K). Seasonal variations in ΔSST are highly correlated with seasonal variations in P_{CENT} in all models with an ensemble mean correlation coefficient of 0.97. The regression coefficient between P_{CENT} and ΔSST is 3.7° K^{-1} in the CMIP3 ensemble average and compares well with that in the observations (3.3° K^{-1}) but varies significantly (standard deviation of 0.7° K^{-1}) between models (Table 2). These results suggest that the robust relationship between seasonal variations in tropical SST gradients and ITCZ location seen in the observations is also found in coupled climate models.

c. Slab ocean aquaplanet simulations

The vast majority of seasonal variations in insolation are stored locally in the ocean (see the discussion in section 2a) and thus the seasonal cycle of energy fluxes in the atmosphere hinges critically on the thermal inertia of the ocean. In this subsection, we analyze the seasonal relationship between ITCZ location and cross-equatorial heat transport in the atmosphere by modifying the amplitude of the seasonal cycle in an ensemble of slab ocean aquaplanet simulation in which the ocean depth is varied from 2.4 to 50 m.

1) MODEL RUNS USED

The model integrations are performed with the Geophysical Fluid Dynamics Laboratory (GFDL) Atmospheric Model version 2.1 (Delworth et al. 2006) featuring a finite-volume dynamical core (Lin 2004) with a horizontal resolution of approximately 2° latitude and 24 vertical levels. The atmospheric model is coupled to a slab ocean with spatially uniform depth. Five ensemble members with prescribed ocean depths of 2.4, 6, 12, 24, and 50 m are analyzed in this study. The model is forced by seasonally varying insolation with zero eccentricity and 23.439° obliquity, and is run for 20 years, sufficient to converge on a steady climatology. The model climatology is taken from the last five years of the integrations.

2) RESULTS

The seasonal migration of the ITCZ off the equator has a larger amplitude for shallower ocean depths (Fig. 8) and P_{CENT} reaches as far as 21° in the 2.4-m slab depth run as compared to 3° in the 50-m slab depth run. This behavior is expected because the adjustment time scale of a 50-m-deep ocean to solar heating is on the order of one year (Donohoe 2011) as compared to weeks for
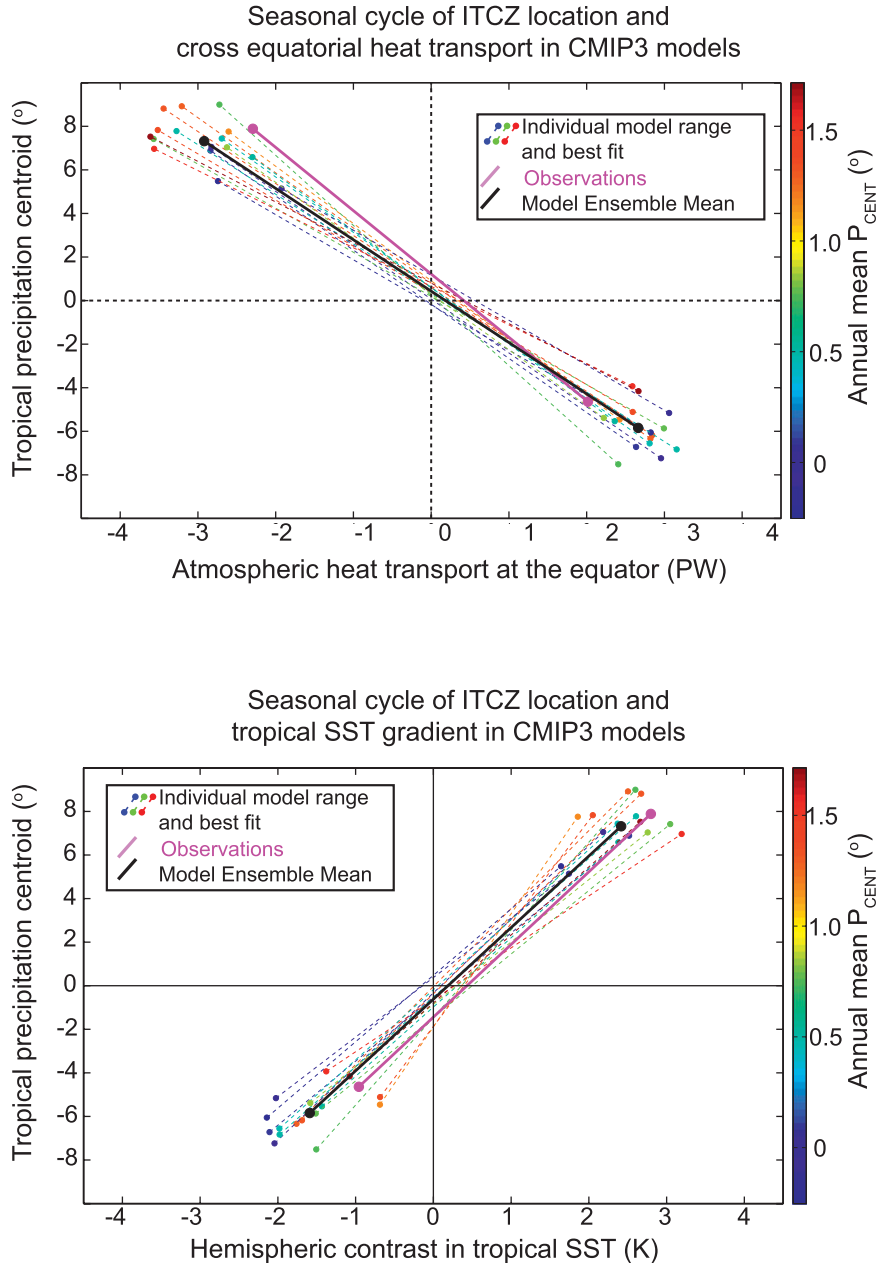
Seasonal cycle of ITCZ location and cross equatorial heat transport in CMIP3 models

Seasonal cycle of ITCZ location and tropical SST gradient in CMIP3 models

FIG. 6. (top) Seasonal range of precipitation centroid vs atmospheric heat transport at the equator (AHT_{EQ}) in individual CMIP preindustrial models (dashed colored lines with filled dots on each end), the model ensemble mean (thick purple line and filled dots), and the observations (thick black line and filled dots). The seasonal range is twice the amplitude of the annual harmonic of each variable and the slope of the line is the regression coefficient of the monthly data. The models are color coded by their annual average P_{CENT} with the color scale given by the color bar to the right. (bottom) As at top, but for precipitation centroid vs interhemispheric contrast of tropical SST.

2.4-m-deep ocean. Thus, the SSTs barely adjust to the seasonally varying insolation in the 50-m run while the maximum SST moves seasonally with the insolation in the 2.4-m run.

The seasonal amplitude of AHT_{EQ} also decreases with increasing ocean depth, from 11.6 PW in the 2.4-m run to 0.5 PW in the 50-m run. In the shallow ocean run, the SSTs respond rapidly to the seasonally varying
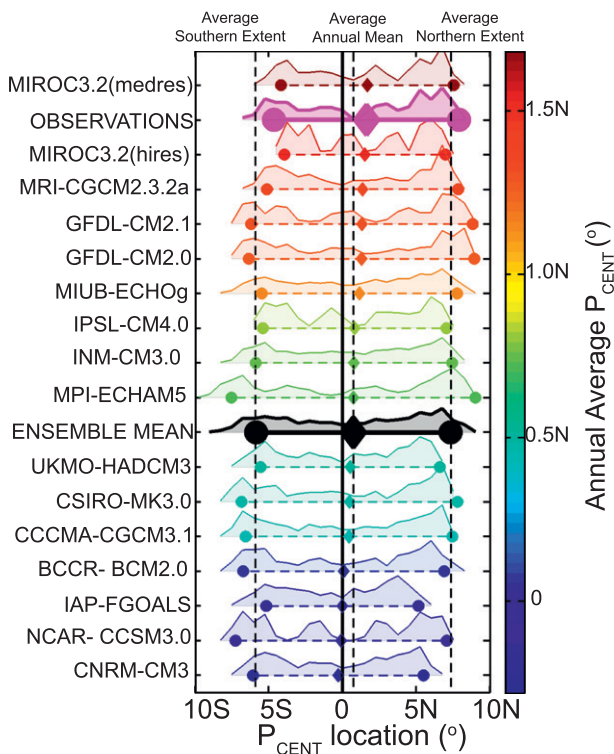
FIG. 7. Histograms of P_{CENT} in the CMIP3 PI models and observations. The shaded region is the normalized histogram of monthly mean P_{CENT} and the seasonal range (defined as twice the amplitude of the annual harmonic) of P_{CENT} is given by the dashed lines attaching the filled dots (representing the climatological northernmost and southernmost extent). The annual average for each model is also shown with the shaded diamond. The models are organized on the y axis and color coded by annual average P_{CENT} with the same color bar used in Fig. 6. Observations are given by the thick magenta line and the CMIP3 ensemble average is shown in the thick black lines. The vertical dashed black lines are the ensemble average annual mean, northernmost, and southernmost extent P_{CENT}.

insolation, heating up over the summer hemisphere and subsequently fluxing energy upward (via turbulent and longwave fluxes) to the adjacent atmosphere to drive seasonal variations in AHT_{EQ}; in the 2.4-m run $\langle SHF \rangle$ is nearly in phase with the insolation (11-day lag) and has a seasonal amplitude of 11.6 PW. In contrast, the solar heating of the ocean makes a minimal impact on ocean temperatures in the deep ocean runs due to the large heat capacity of the ocean. In fact, SWABS is the only source of seasonal atmospheric heating in the 50-m run and the atmosphere loses energy to the ocean during the warm season; in the 50-m run $\langle SHF \rangle$ is nearly antiphased with the insolation (192-day lag) and has a seasonal amplitude of 3.7 PW.

Seasonal variations in P_{CENT} and AHT_{EQ} are strongly anticorrelated, with an ensemble average correlation

coefficient of -0.95. The relationship between seasonal variations in P_{CENT} and AHT_{EQ} changes with mixed layer depth (cf. the slopes in Fig. 8). The linear best fit to the monthly averaged data has a slope of $-2.0°$ PW^{-1} in the 2.4-m run and $-6.1°$ PW^{-1} in the 50-m run and varies monotonically with ocean depth for the intermediate depth runs. This result is not expected from our conceptual model of the mutual dependency of the ITCZ location and atmospheric heat transport on meridional shifts in the Hadley cell (Fig. 1). We argue that the decrease in the slope of P_{CENT} with respect to AHT_{EQ} as the ocean depth decreases is a consequence of the following two factors:

1) The maximum upward motion (and convective precipitation) occurs where the meridional gradient of the overturning streamfunction is greatest by the (Boussinesq) continuity equation. For a symmetric Hadley circulation (with summer and winter cells of equal magnitude), the upward motion will be centered about the location of the zero streamfunction. In contrast, in a nonsymmetric Hadley circulation where the winter cell is more intense than the summer cell, the location of maximum streamfunction gradient occurs within the winter cell and the maximum upward motion and precipitation occurs equatorward of where the streamfunction goes to zero. For example, in the 2.4-m run, P_{CENT} is nearly collocated with the location of maximum streamfunction gradient (cf. the dashed light blue line in the lower panel of Fig. 9 with the dashed green line) for all months and the seasonal migration of the streamfunction zero crossing is nearly twice as large (the dashed black line); the regression coefficient between seasonal variations in the P_{CENT} and the location of maximum streamfunction gradient is 0.95 whereas the regression coefficient between P_{CENT} and the streamfunction zero crossing is 0.42. In contrast, in the 50-m depth run, the ITCZ stays close to the equator and the winter and summer Hadley cells are nearly mirror images of one another. As a consequence, P_{CENT} is nearly collocated with both the location of maximum streamfunction derivative and the streamfunction zero crossing over the seasonal cycle (regression coefficients of 0.88 and 0.86, respectively). In summary, the precipitation centroid has less meridional migration than the overturning streamfunction as the ITCZ moves farther from the equator and an asymmetry between the magnitude of the winter and summer cells develops.

2) The winter Hadley cell increases in intensity (relative to the summer cell) as the ITCZ moves farther off the equator. As a consequence, the cross-equatorial

Seasonal cycle of ITCZ location and cross equatorial heat transport in slab aquaplanet simulations
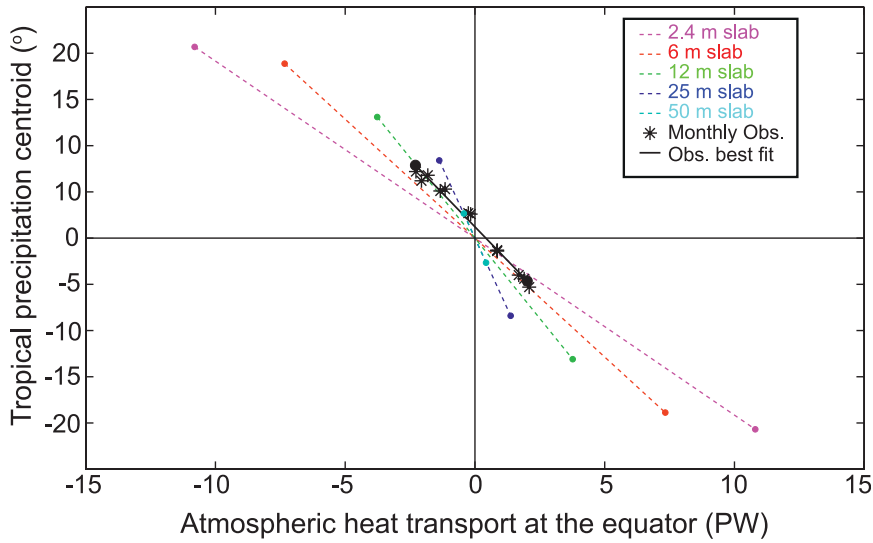
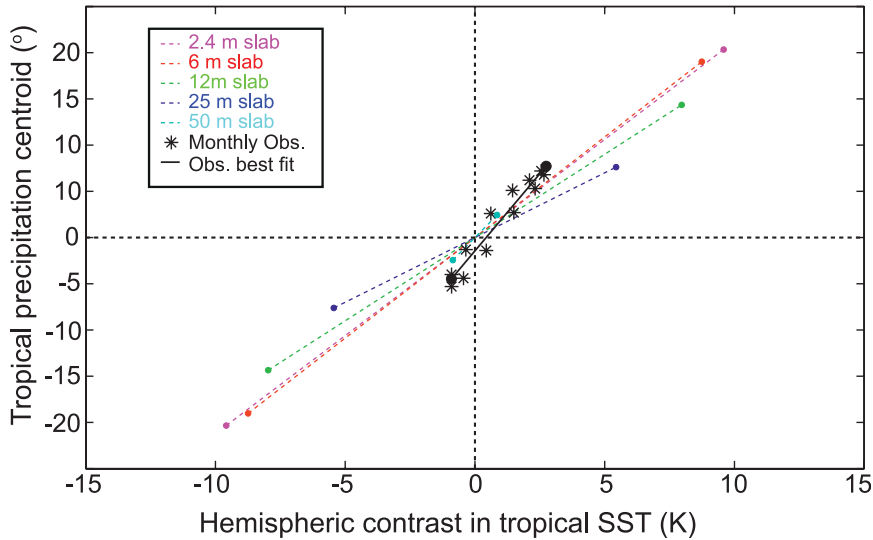## Seasonal cycle of ITCZ location and hemispheric contrast of tropical SST

FIG. 8. (top) Seasonal range of precipitation centroid and atmospheric heat transport across the equator in the slab ocean aquaplanet simulations with each simulation (ocean depth) given by a different color. The seasonal range is twice the amplitude of the annual harmonic of each variable and the slope of the line is the regression coefficient of the monthly data. The black asterisks are the monthly observations and the solid black line is the seasonal range of the observations. (bottom) As at top, but for precipitation centroid and tropical SST gradient.

heat transport in the atmosphere changes more than would be expected from meridionally translating the Hadley cell without concurrently changing the structure/intensity of the cells as the ITCZ moves off the equator.

As a result of the two above factors, when the ITCZ moves farther from the equator (and the winter cell intensifies relative to the summer cell), the precipitation centroid moves less than would be expected from meridionally translating the Hadley circulation and the heat
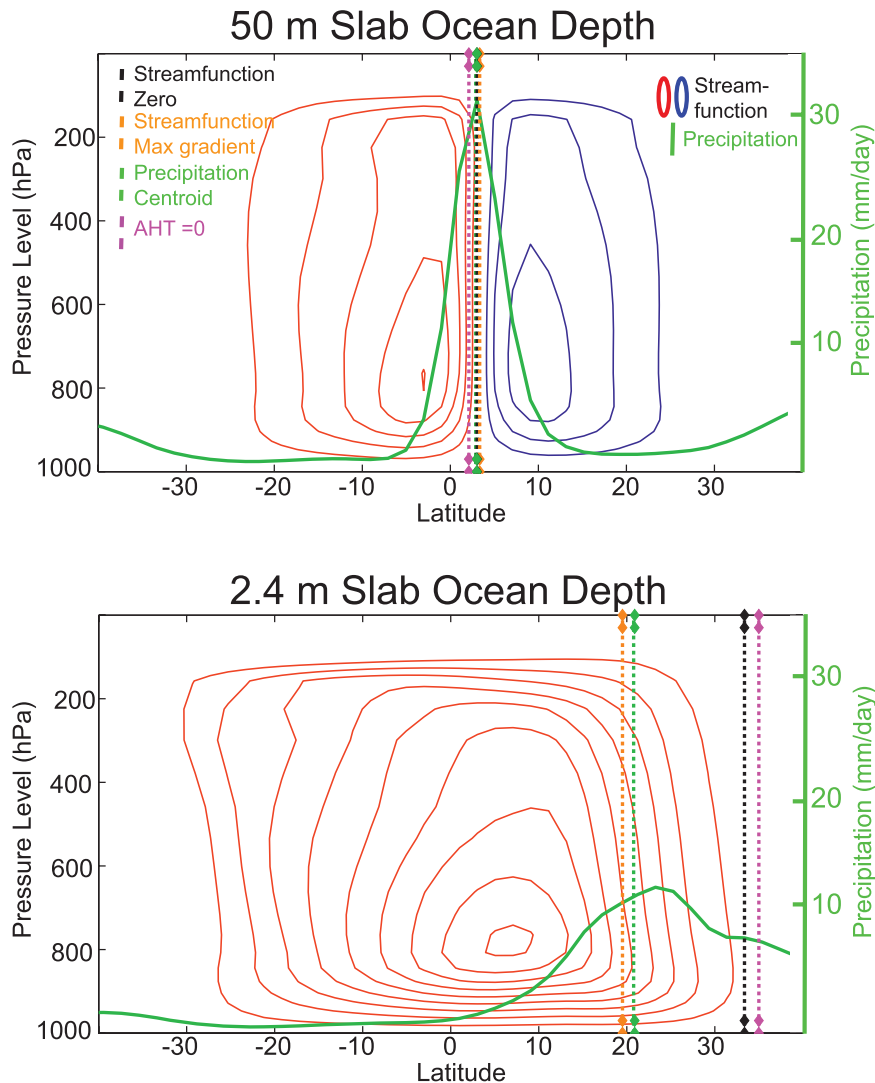
FIG. 9. Boreal summer meridional overturning streamfunction in the atmosphere (red and blue contours with a contour interval of 50 Sv) coplotted with the zonal mean precipitation (solid green lines). Also shown is the precipitation centroid (dashed green line), the location where the AHT is 0 (dashed purple line), the location of the 0 streamfunction at 600 hPa (dashed black line), and the location of maximum streamfunction gradient at 600 hPa (dashed orange line). The top panel is 50-m slab ocean run and the bottom panel is the 2.4-m slab ocean run.

transport across the equator changes more than would be expected. The net result is that the slope of P_{CENT} with respect to AHT_{EQ} decreases as the ITCZ moves off the equator. Indeed, in the 2.4-m slab depth simulation, the relationship between P_{CENT} and AHT_{EQ} follows the same steep sloped line found in the 50-m run for the transition (fall and spring) months when the ITCZ crosses the equator (not shown).

The relationship between P_{CENT} and AHT_{EQ} in the observations is coplotted with the slab ocean

aquaplanet simulations in Fig. 8. The slope found in the observations is very close to that of the 24-m depth run while the seasonal amplitude of P_{CENT} and AHT_{EQ} in the observations falls somewhere between that in the 6-m and 12-m runs. We will return to a discussion of these points in section 4.

The seasonal amplitude of ΔSST increases with decreasing slab ocean depth, from 0.9 K in the 50-m run to 9.6 K in the 2.4-m run. Seasonal variations in ΔSST are significantly correlated with those in P_{CENT} in all runs

but the correlations are weaker than those between P_{CENT} and AHT_{EQ} and decrease to an R^2 of 0.67 in the 50-m run. The latter is a consequence of a phase lead of ΔSST relative to P_{CENT} that increases with increasing mixed layer depth to 36 days for the 50-m run. In contrast, P_{CENT} and AHT_{EQ} are nearly antiphased in all runs with an average phase difference magnitude of 11 days. The regression coefficient between P_{CENT} and ΔSST varies nonmonotonically with slab depth and reaches a maximum of $2.9°\,K^{-1}$ in the 24-m run and a minimum of $1.4°\,K^{-1}$ in the 50-m run with an ensemble average of $2.1°\,K^{-1}$.

3. ITCZ shifts and cross-equatorial atmospheric heat transport change due to anthropogenic and paleoclimatic forcing

The previous section demonstrated that there is a robust and consistent relationship between the P_{CENT} and AHT_{EQ} and between P_{CENT} and ΔSST over the seasonal cycle in both observations and coupled climate models. We now analyze the relationship between annual mean shifts in ITCZ location and change in AHT_{EQ} and ΔSST due to anthropogenic and paleoclimatic forcing. We argue that the same quantitative relationships found in the seasonal cycle also apply to the climate change problem across a myriad of different forcings.

a. Model runs analyzed

1) CARBON DIOXIDE DOUBLING EXPERIMENTS

We analyze the CMIP3 1% CO_2 increase to doubling experiments (Meehl et al. 2007). Each model is initialized from the equilibrated preindustrial (PI) or in some cases [CCSM, the Meteorological Research Institute (MRI) model, and ECHAM] the present-day (PD) simulations. Atmospheric carbon dioxide increases at a rate of 1% per year until it has doubled (at year 70) and is then held fixed for an additional 150 years of simulations. We calculate the climatology of each model over the last 20 years of simulations and then take differences relative to the climatology in the PI (or PD) run. We will refer to these runs as the $2XCO_2$ runs. Fifteen different models are analyzed.

2) LAST GLACIAL MAXIMUM SIMULATIONS

We utilize model output from phase 2 of the Paleoclimate Modeling Intercomparison Project (PMIP2), an ensemble of state-of-the-art coupled (ocean–atmosphere–cryosphere) model simulations run under prescribed forcing and boundary condition scenarios that represent different paleoclimatic epochs. The Last Glacial Maximum (LGM) simulations are forced by insolation from 21 000 years before present, with greenhouse gas and aerosol concentrations deduced from ice core data (CO_2 is set to 185 ppm), which amounts to a radiative forcing of approximately $-2.8\,W\,m^{-2}$ (Braconnot et al. 2007a), coastlines consistent with a 120-m decrease in sea level, and the prescribed land ice topography of Peltier (2004), which includes the expansive Laurentide ice sheet over North America. We use the LGM simulations with fixed vegetation (PMIP2 OA runs). All comparisons are made to the preindustrial simulations in the same model and resolution (many of which are lower resolution than the PI simulations analyzed in section 2b). Seven different model simulations are analyzed.

3) 6000 YEARS BEFORE PRESENT SIMULATIONS

The PMIP2 mid-Holocene runs are used (Braconnot et al. 2007a). We will refer to these experiments as the 6Kyr runs. Coastlines, vegetation, and ice sheets are identical to the PI simulations. CO_2 and aerosols are also identical to the PI while there is a modest reduction in methane concentration (from 760 to 650 ppbv). Orbital parameters representative of 6000 years before the present are taken from Berger and Loutre (1991). Most significantly, orbital precession causes the seasonal cycle of insolation in the Northern Hemisphere to amplify, while the duration of summer is reduced; the seasonal amplitude of $\langle SW_{\downarrow,TOA}\rangle$ increases by 2.5% relative to the PI climate. Enhanced obliquity causes more high-latitude insolation in the annual mean. We note that the sum of all mid-Holocene forcing agents is symmetric about the equator in the annual average. Six different model simulations of 6Kyr are analyzed.

b. Results

We present the results across all three forcing experiments here, and then further analyze the $2XCO_2$, LGM, and 6Kyr experiments in sections 3b(1)–3b(3). The change in annual mean P_{CENT} in the three forcing experiments is plotted against the change in annual mean AHT_{EQ} and ΔSST in the top and bottom panels of Fig. 10, respectively. In the LGM and $2XCO_2$ experiments the intermodel spread in both the change in P_{CENT} and AHT_{EQ} is larger than the ensemble average change and so the sign of the change is ambiguous (cf. the solid red and blue squares with the spread in the red and blue crosses across both axes); the ensemble average change in P_{CENT} and AHT_{EQ} is not significantly different from zero in the LGM and $2XCO_2$ runs. This result is surprising, especially in the LGM case, where one would expect that the large Laurentide ice sheet in the Northern Hemisphere would lead to a deficit of absorbed shortwave radiation (a positive change $\langle SW_{NET,TOA}\rangle$) leading to a cooling in the Northern Hemisphere (relative to the Southern Hemisphere), a decrease in ΔSST,
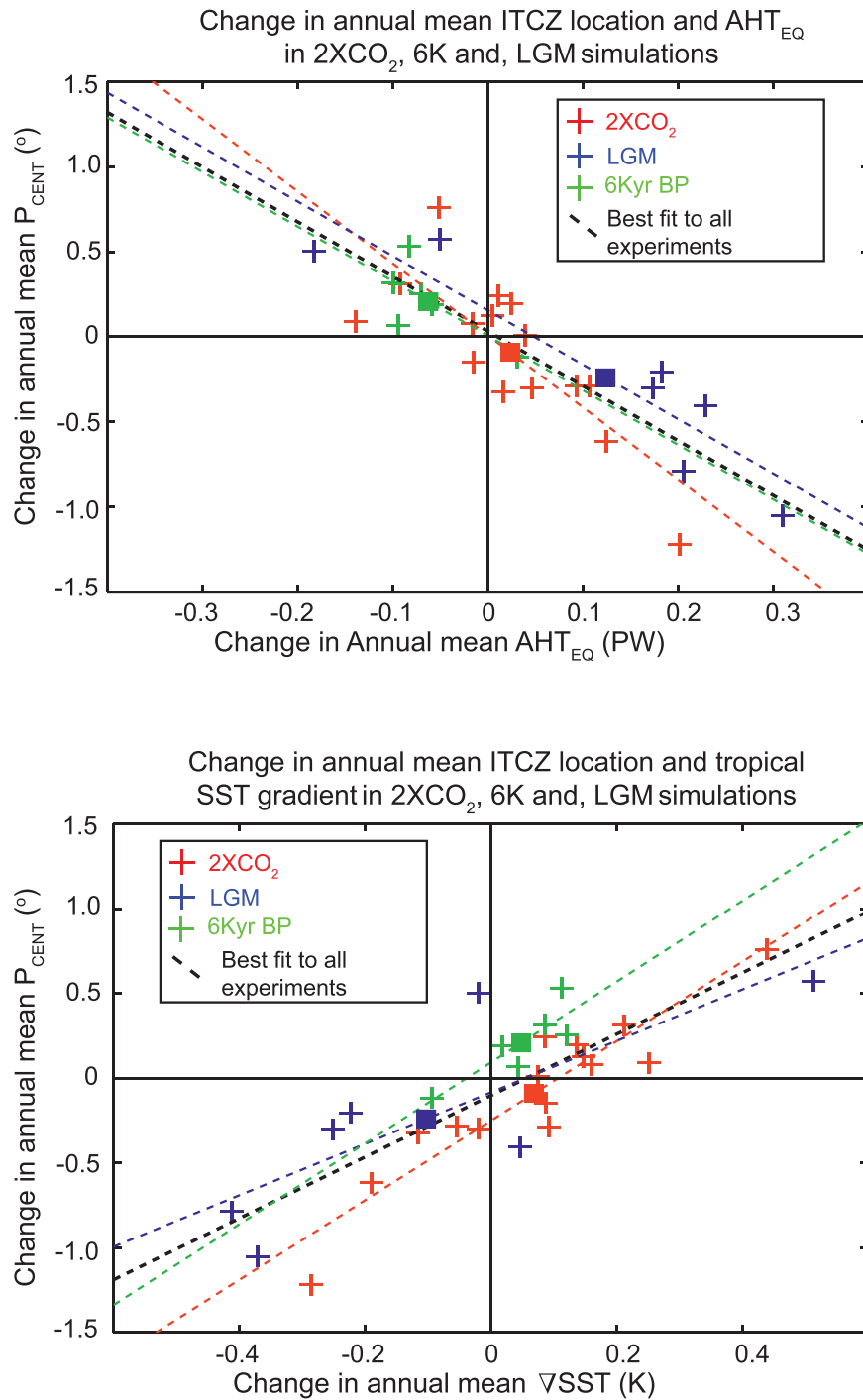
FIG. 10. (top) Change in annual mean precipitation centroid vs change in cross-equatorial heat transport in the atmosphere in the $2XCO_2$ simulations (each red cross is a different ensemble member), 6000 years before present simulations (green crosses), and Last Glacial Maximum simulation (blue crosses). The dashed red, green, and blue lines are the linear best fits in the $2XCO_2$, 6Kyr, and LGM runs, respectively. The dashed black line is the linear best fit to all experiments. The filled boxes are the ensemble mean of each simulation. (bottom) As at top, but for change in annual mean precipitation centroid (P_{CENT}) vs change in tropical SST gradient (ΔSST).

a southward shift in P_{CENT}, and more northward AHT_{EQ}. This result suggests that intermodel differences in the spatial structure of climate feedbacks can play a bigger role in setting the interhemispheric contrast of the temperature and energetic response than does the interhemispheric contrast in climate forcing and boundary conditions themselves.

In contrast to the LGM and $2XCO_2$ experiments, in the 6Kyr simulations there is a significant (99% confidence interval) ensemble average northward shift of P_{CENT} of 0.21°, a decrease (more southward) in AHT_{EQ} of −0.06 PW, and a 0.06 K increase in ΔSST (Table 3). Despite the lack of significance of the ensemble average changes in the $2XCO_2$ and LGM experiments, the ensemble average changes in P_{CENT} and AHT_{EQ} are consistent with the relationship found in the seasonal cycle in section 2; the ensemble average southward shift of the ITCZ in the LGM is accompanied by a more northward AHT_{EQ} while the ensemble average northward ITCZ shift in the 6Kyr experiment is accompanied by more southward AHT_{EQ} (and the ensemble average $2XCO_2$ change is more neutral) with a quantitative relationship of approximately −3° PW^{-1}. In contrast, the robust relationship between P_{CENT} and ΔSST found in the seasonal cycle does not predict the ensemble average ITCZ shift in the $2XCO_2$ runs. Here the increase in ΔSST is accompanied by a southward shift in P_{CENT}.

In each experiment, the change in annual mean P_{CENT} and AHT_{EQ} changes are significantly negatively correlated among the ensemble members with an average correlation coefficient of −0.81 and a correlation coefficient of −0.85 when considering all experiments collectively. The regression coefficient between P_{CENT} and AHT_{EQ} ranges from −4.2° PW^{-1} in the $2XCO_2$ ensemble to −3.2° PW^{-1} in the LGM and 6Kyr ensembles (Table 3) and the regression coefficient of all simulations considered simultaneously is −3.2° PW^{-1}. These relationships are in good agreement with the seasonal slope between P_{CENT} and AHT_{EQ} of −2.7° PW^{-1} found in the observations. These results collectively suggest that the relationship between P_{CENT} and AHT_{EQ} is robust across time scales (seasonal vs annual mean) and across different climate states. We return to this point in the discussion section.

The intermodel spread in annual mean P_{CENT} and ΔSST changes are significantly positively correlated in all three perturbation experiments with an average correlation coefficient of 0.86 and a slope that ranges from +1.5° K^{-1} in the LGM simulations to +2.4° K^{-1} in the 6Kyr experiments (Table 3). These slopes are significantly shallower but of similar magnitude to that found in the seasonal cycle in the observations (+3.3° K^{-1}).

TABLE 3. Ensemble average, spread (1σ), and regression coefficients for P_{CENT}, AHT_{EQ}, and ΔSST in the $2XCO_2$, LGM, and 6Kyr experiment.

	$2XCO_2$	LGM	6Kyr
Ensemble avg change in P_{CENT} (°)	−0.09	−0.24	+0.21
Ensemble spread (1σ) of change in P_{CENT} (°)	0.46	0.61	0.22
Ensemble avg change in AHT_{EQ} (PW)	+0.02	+0.12	−0.06
Ensemble spread (1σ) of change in AHT_{EQ} (PW)	0.09	0.17	0.05
Ensemble avg change in ΔSST (K)	+0.06	−0.10	+0.06
Ensemble spread (1σ) of change in ΔSST (PW)	0.18	0.32	0.07
Regression coef between change in P_{CENT} and AHT_{EQ} (° PW^{-1})	−4.2	−3.2	−3.2
Regression coef between change in P_{CENT} and ΔSST (° K^{-1})	+2.3	+1.5	+2.4

1) $2XCO_2$ EXPERIMENTS

The ITCZ response to CO_2 doubling in the CMIP3 slab ocean simulations was analyzed thoroughly by Frierson and Hwang (2012), who concluded that there are large intermodel differences in the annual mean ITCZ shift due to differences in the AHT_{EQ} change that primary reflect intermodel differences in extratropical feedbacks. We find a similar relationship between P_{CENT} and AHT_{EQ} in the coupled 1% CO_2 increase runs. The ensemble average 0.02 PW increase AHT_{EQ} in the $2XCO_2$ simulations analyzed in this study is decomposed into a nearly compensating 0.22 PW increase in $\langle SW_{NET,TOA} \rangle$ [associated with increased cloudiness in the Northern Hemisphere midlatitudes as assessed by the method of Donohoe and Battisti (2011)] and a 0.29 PW increase in $\langle OLR \rangle$ (associated primarily with the Planck feedback and larger temperature increases in the Northern Hemisphere as compared to those in the Southern Hemisphere). Additionally, there is a 0.09 PW decrease in $\langle OHT + S \rangle$, which implies either more southward ocean heat transport or more transient heat storage in the Northern Hemisphere as compared to the Southern Hemisphere. We emphasize that the ensemble average change in the hemispheric contrast of the energy budget due to CO_2 doubling is small compared to the intermodel spread as pointed out by Zelinka and Hartmann (2012) and Frierson and Hwang (2012). Furthermore the ITCZ shift due to anthropogenic climate forcing varies in sign between models and depends critically on extratropical climate feedbacks.

2) LGM EXPERIMENTS

The most pronounced change in the interhemispheric energy budget in the LGM is the presence of the Laurentide ice sheet in the Northern Hemisphere; the cryosphere expanded drastically in the Northern Hemisphere and only modestly in the Southern Hemisphere during the LGM. The ensemble average spatially and solar weighted surface albedo of the Northern Hemisphere increased by 0.029 relative to that in the Southern Hemisphere (with an ensemble standard deviation of 0.018 due to differences in the albedo of the Laurentide ice sheet), which translates to an increase in $\langle SW_{NET,TOA} \rangle$ of +1.30 PW if the same surface albedo change was found in the planetary albedo. However, the shortwave atmospheric opacity limits the surface albedo's impact on the TOA radiative budget while decreased cloudiness over the ice sheet compensates for the increased surface reflection and the ensemble average change in $\langle SW_{NET,TOA} \rangle$ is +0.43 PW (and ranges from +0.03 to +0.84 PW in the ensemble members). Using the method of Donohoe and Battisti (2011) to partition the planetary albedo into contributions from surface albedo and cloud reflection, we find that the ensemble average change in $\langle SW_{NET,TOA} \rangle$ is due to a +0.60 PW contribution from changes in surface albedo and a −0.17 PW contribution from changes in atmospheric reflection (fewer clouds over the ice sheet).

The deficit of absorbed shortwave radiation in the Northern Hemisphere (a positive change in $\langle SW_{NET,TOA} \rangle$) leads to a cooling of the Northern Hemisphere (relative to the Southern Hemisphere) and must either be balanced radiatively by decreased OLR ($\langle OLR \rangle$), or dynamically by increasing either atmospheric (AHT_{EQ}) or oceanic heat transport and storage ($\langle OHT + S \rangle$). The ensemble average 0.43 PW increase $\langle SW_{NET,TOA} \rangle$ (i.e., less shortwave radiation absorbed in the Northern Hemisphere) is balanced primarily by a 0.32 PW increase in $\langle OLR \rangle$ (i.e., a decrease in OLR in the Northern Hemisphere), secondarily by a 0.12 increase in AHT_{EQ} and is slightly opposed by a 0.01 PW decrease in $\langle OHT + S \rangle$. Intermodel differences in $\langle SW_{NET,TOA} \rangle$ are well correlated with both intermodel differences in $\langle OLR \rangle$ and AHT_{EQ} (with correlations coefficients of 0.88 and 0.87, respectively) with nearly equal magnitude regression coefficients. These results suggest that the deficit in absorbed shortwave radiation in the Northern Hemisphere induced by the Laurentide ice sheet is primarily balanced radiatively (by OLR anomalies) and only secondarily by dynamics (atmospheric heat transport changes), with less than half of the shortwave anomaly being realized in the atmospheric heat transport change. In summary, the rather large interhemispheric contrast in energetics induced by

the Laurentide ice sheet's albedo (1.30 PW) is largely damped by 1) the factor of approximately 2.5 attenuation of the surface albedo's impact on the TOA energy budget by the atmospheric shortwave opacity, 2) compensating decreases in cloudiness over the Laurentide ice sheet, and 3) radiative compensation via the Planck feedback. As a result, approximately 10% (0.12 PW) of the energetics implied by the surface albedo changes are realized in cross-equatorial atmospheric heat transport, resulting in a very modest ensemble average shift in the ITCZ location.

Braconnot et al. (2007b) previously demonstrated the surprising result that, in PMIP2 LGM simulations, the meridional shift of the ITCZ during the boreal summer differs in sign between the ensemble members. We find here that indeed, and contrary to expectations, two models shift the annual mean ITCZ toward the Northern Hemisphere. We note that, in both cases, these changes are expected given the change in AHT_{EQ} and the relationship between P_{CENT} and AHT_{EQ}. We now discuss the cause of the negative (more southward) change in AHT_{EQ} in these two models. In ECHAM5, $\langle SW_{NET,TOA} \rangle$ increases by 0.24 PW, primarily due to the surface albedo change, and $\langle OLR \rangle$ increases by 0.46 PW, primarily due to the Planck feedback and more cooling in the Northern Hemisphere as compared to the Southern Hemisphere. Because the $\langle OLR \rangle$ change is larger in magnitude than the $\langle SW_{NET,TOA} \rangle$ change, the ice sheet actually introduces a net source of energy to the atmosphere in the Northern Hemisphere due to radiative overcompensation and AHT_{EQ} moves energy away from the energy source in the Northern Hemisphere, resulting in a northward ITCZ shift. In FGOALS, the total heat transport across the equator is nearly unchanged (−0.05 PW) due to a large radiative compensation with the change in $\langle SW_{NET,TOA} \rangle$ being nearly, but not completely balanced by $\langle OLR \rangle$. Concurrently, $\langle OHT + S \rangle$ increases by 0.10 PW either due to more northward ocean heat transport or transient energy storage in the Southern Ocean. As a consequence, AHT_{EQ} decreases by 0.05 PW, largely reflecting compensation between oceanic and atmospheric heat transport, and the ITCZ shifts northward.

3) 6KYR EXPERIMENTS

The robust annual mean northward ITCZ shift and more southward AHT_{EQ} in the 6Kyr runs is surprising given that there is no interhemispheric contrast of forcing in the annual mean and implies that nonlinearities in the seasonal response to forcing play a vital role in setting the ITCZ location. In the ensemble average, the changes in net radiation at the TOA have a minimal impact on AHT_{EQ} as the 0.06 PW increase in $\langle SW_{NET,TOA} \rangle$ (associated with reduced cloudiness in the Northern

Hemisphere midlatitudes) is nearly balanced by a 0.05 PW increase in $\langle \text{OLR} \rangle$ (associated with warming of the northern subtropics). Ultimately, the ensemble average 0.06 PW decrease (more southward) in AHT_{EQ} is a consequence of a 0.07 increase in $\langle \text{OHT} + S \rangle$. Our analysis techniques cannot distinguish between a change in cross-equatorial ocean heat transport and a hemispheric asymmetry of transient ocean storage. The annual mean shift in the 6Kyr runs reflects the ITCZ moving farther northward during the boreal summer while the ITCZ migration into the Southern Hemisphere during the austral summer is nearly unchanged relative to that in the PI simulations, as discussed further in our concluding remarks.

4. Summary and discussion

The seasonal cycle of the location of the ITCZ (P_{CENT}) is highly anticorrelated with the atmospheric heat transport at the equator (AHT_{EQ}) and highly correlated with the interhemispheric contrast of tropical sea surface temperatures (ΔSST) in both the observations ($R^2 = 0.99$ and 0.94 respectively) and coupled climate models ($R^2 = 0.80$ and 0.94 respectively). We argue that the relationship between P_{CENT} and AHT_{EQ} is a consequence of their mutual association with the meridional migration of the Hadley cell. The regression coefficient between P_{CENT} and AHT_{EQ} over the seasonal cycle is $-2.7° \, \text{PW}^{-1}$ in the observations and agrees well with the CMIP3 ensemble average of $-2.4° \, \text{PW}^{-1}$. Similarly, the regression coefficient between P_{CENT} and ΔSST over the seasonal cycle is $+3.3° \, \text{K}^{-1}$ in the observations and agrees well with the CMIP3 ensemble average of $+3.7° \, \text{PW}^{-1}$.

The annual mean shift in ITCZ (P_{CENT}) across a myriad of climate forcing experiments (2XCO$_2$, LGM, and mid-Holocene) in coupled climate models is well correlated with the change in AHT_{EQ} with a regression coefficient of $-3.2° \, \text{PW}^{-1}$, in excellent agreement with that found over the seasonal cycle. This result suggests that the same physics that control the seasonal cycle of AHT_{EQ} and P_{CENT}, via their mutual connection to the Hadley cell, also control changes in the annual mean.

The seasonal relationship between P_{CENT} and AHT_{EQ} was found to depend on how far off the equator the ITCZ moves in a series of aquaplanet simulations with varying mixed layer depth. We argue that the asymmetry between the winter and summer Hadley cells is critical to this result due to two processes: 1) AHT_{EQ} changes more than would be expected from simply translating the annual mean Hadley cell off the equator due to the intensification of the streamfunction in the winter cell as the Hadley cell moves off the equator, and 2) the ITCZ remains equatorward of the zero

streamfunction because the maximum meridional divergence of the streamfunction and upward motion gets pushed into the winter cell due to the asymmetry between the winter and summer Hadley cells. As a consequence, the AHT_{EQ} change required per degree shift in the ITCZ increases as the ITCZ moves farther off the equator. We note that, in the annual average, the ITCZ is relatively close to the equator and the two branches of the Hadley cell are nearly symmetric as compared to the seasonal extremes. This might lead one to believe that the AHT_{EQ} change required to move the ITCZ 1° would be comparable to that expected from simply translating the Hadley cell meridionally without the concurrent intensification of the winter cell (on the order of 0.1 PW; see red asterisks in Fig. 5) and less than that found over the seasonal cycle (on the order of 0.3 PW; see upper panel of Fig. 3). Yet, we concluded above that the relationship between P_{CENT} and AHT_{EQ} over the observed seasonal cycle is statistically indistinguishable from the relationship found for the annual mean changes across the ensemble of climate change perturbation experiments. We argue below that the seasonal relationships between P_{CENT} and AHT_{EQ} is dictated by the seasonal cycle because the annual average is seldom realized and is better thought of as the average of the seasonal extremes (and the amount of time spent in the extreme) as illustrated in Fig. 7.

The top panel of Fig. 11 shows smoothed histograms (Eilers and Goeman 2004) of monthly mean P_{CENT} and AHT_{EQ} for 200 years of the PI simulation in the IPSL model. The annual mean (black cross) is seldom realized and the system rapidly migrates between seasonal extremes of P_{CENT} in the Northern Hemisphere and southward AHT_{EQ} in the boreal summer and P_{CENT} in the Southern Hemisphere and northward AHT_{EQ} in the austral summer. The linear best fit (dashed black line) connects the seasonal extremes with a slope equal to the regression coefficient between P_{CENT} and AHT_{EQ} and nearly passes through the origin. By statistical construction, the annual mean lies on the linear best fit line. In short, the annual mean reflects the average of the two seasonal extremes.[4]

The smoothed histogram and linear best fit of P_{CENT} and AHT_{EQ} for the IPSL 2XCO$_2$ simulation are very similar to their PI counterparts (middle panel of Fig. 11). However, during both seasonal extremes, P_{CENT} has

---

[4] We note that, in this particular case, the time spent in the boreal and austral summer extremes is approximately equal (the lobes of the smoothed histogram are comparable in magnitude) and the annual mean falls nearly equidistant from the extremes. If more time was spent in either of the seasonal extremes, the lobes would have different magnitudes and the annual mean would be shifted toward the more populated lobe.

shifted southward and there is more northward AHT_{EQ}. As a consequence, the annual average P_{CENT} and AHT_{EQ} have also shifted in the same sense as the seasonal extremes. The key point is that, provided that the seasonal relationship between P_{CENT} and AHT_{EQ} is consistent between climate states, *the annual mean shifts along the seasonal linear best fit; the relationship between annual mean shift in P_{CENT} and AHT_{EQ} will be the same as the relationship between P_{CENT} and AHT_{EQ} found over the seasonal cycle.* We extend this analysis to the LGM and 6Kyr runs alongside the PI and $2XCO_2$ in the bottom panel of Fig. 11 where a single smoothed histogram contour $[2.5\% \ (^{\circ} \ PW)^{-1}]$ is shown for visual purposes. There we see that while the shift from the PI to $2XCO_2$ is apparent in both seasons, in the 6Kyr run the boreal summer extreme shifts farther away from the origin (along the seasonal slope) while the austral summer statistics are relatively unchanged. In contrast, in the LGM the ITCZ and AHT_{EQ} are relatively unchanged during the boreal summer while, in the austral summer, the ITCZ shifts more southward and the AHT_{EQ} becomes more northward. In all cases, the asymmetric shifting of the seasonal extremes result in a shift of the annual mean and, most importantly, *the annual mean shifts along the seasonal slope between P_{CENT} and AHT_{EQ}.*

Our framework suggest that perturbations to the interhemispheric asymmetry of atmospheric energy budget [Eq. (4)] at *all latitudes* and from *all sources* (e.g., ocean heat transport anomalies, surface heat flux anomalies, and radiative perturbations) have an equal impact on AHT_{EQ} and on the ITCZ location via the connection between P_{CENT} and AHT_{EQ}. Similar ideas have been expressed by Chiang and Bitz (2005), Kang et al. (2008), Frierson and Hwang (2012), and Yoshimori and Broccoli (2008), among others. In contrast, there is an abundance of literature on the role of tropical processes in setting the ITCZ location including the coastal geometry (Philander et al. 1996), the roles of the Andes is shaping the spatial structure of SST (Takahashi and Battisti 2007), and the role of the tropical oceanic circulation (Clement and Seager 1999), among others. We note that, while our results speculate that extratropical energy inputs play a vital role in setting and shifting the ITCZ location, we have not demonstrated causality. The interhemispheric energy budget must come into balance with AHT_{EQ} changes that accompany ITCZ shifts and the resulting radiative and surface heat flux anomalies could be a manifestation of changes in the tropics.

Our results have implications for ITCZ location in paleoclimate states, some of which have already been discussed in the context of the PMIP2 models (section 3). In particular, paleoclimate records have been used to deduce ITCZ shifts and, in some cases, have been used
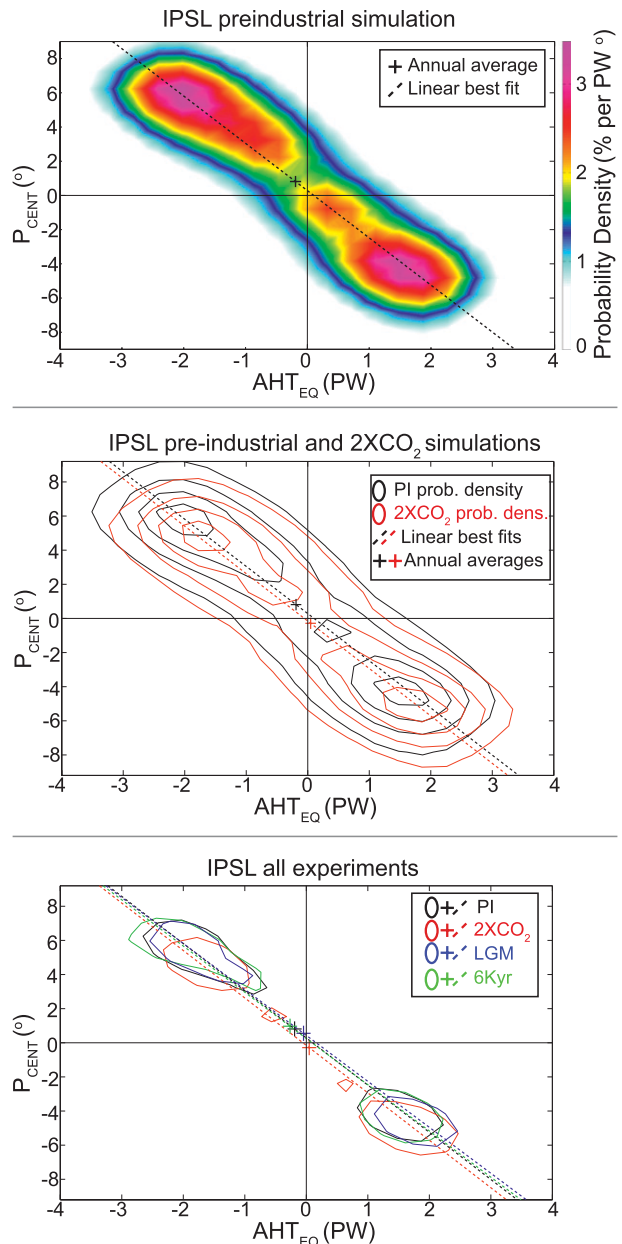

FIG. 11. (top) Smoothed histogram (colors) in the AHT_{EQ}–P_{CENT} plane taken from a 200-yr-long PI simulation in the L'Institut Pierre-Simon Laplace (IPSL) model. The dashed line is the linear best fit to the monthly data for all years of the simulation and the cross is the annual average. (middle) As at top, but the probability density function is contoured [contour interval of $0.75\% \ (^{\circ} \ PW)^{-1}$] with black contours showing the PI values and red values showing the $2XCO_2$ values. The red and black crosses and dashed lines represent the annual average and linear best fits in the $2XCO_2$ and PI simulations respectively. (bottom) As in the middle panel except only the $2.5\% \ (^{\circ} \ PW)^{-1}$ contour is shown. The PI simulation is shown in black, $2XCO_2$ in red, LGM in blue, and the 6Kyr simulation in green.

to quantify bounds on meridional position of the ITCZ (i.e., Sachs et al. 2009) over Earth's history. The quantitative scaling of the relationship between ITCZ position and AHT_{EQ} found in this study allows one to infer the change in cross-equatorial atmospheric heat transport implied by the paleoclimate reconstructions of ITCZ location, and ultimately relate these quantities back to the hemispheric-scale energy budget (Fig. 2) of the climate system. For example, the southward ITCZ shift on the order of 5° during the Little Ice Age suggested by Sachs et al. (2009) implies an AHT_{EQ} change of approximately 1.7 PW; presently, there is no known climate forcing or feedback during that time period that could account for such a large energy perturbation at the hemispheric scale. Similarly, the same ITCZ shift would be associated with a ΔSST change within the range of 1.5–3.7 K (using the range of regression coefficients between P_{CENT} and ΔSST found in this study) that ought to be readily seen in proxy SST reconstructions. We view the relationship between P_{CENT} and AHT_{EQ} to be fundamental to the system because of the mutual dependence of the tropical rainfall and the atmospheric heat transport on the Hadley cell; we expect this relationship to hold from one climate state to the next because the seasonal anomalies are large compared to the climate perturbations and thus the seasonal cycle captures the system behavior to a fairly wide range of climate forcings. In contrast, we view the relationship between ITCZ location and ΔSST as empirical and potentially variant to the climates. However, ΔSST may be easier to constrain from paleo data and, thus, its relationship to the ITCZ location could help to place paleo observations into the framework presented in this manuscript.

Our analysis has focused on the zonal mean tropical precipitation and atmospheric heat transport. Clearly, paleoclimate records are indicative of more localized climate changes; the ITCZ shifts noted by Sachs et al. (2009) are derived from data along a latitudinal transect over a given longitudinal band in the Pacific. It remains to be seen if the diagnostics used in this study are applicable to more localized records as would be the case if ITCZ movements were zonally homogeneous, as suggested by Frierson and Hwang (2012). In future work, we hope to assess if the relationships among ITCZ location, AHT_{EQ}, and ΔSST found in this study can be applied to specific paleoclimate reconstructions in order to deduce past changes in the large-scale atmospheric circulation and the energetic processes responsible for those changes.

REFERENCES

Berger, A., and M. Loutre, 1991: Insolation values for the climate of the last 10 million years. *Quat. Sci. Rev.,* **10,** 297–317.

Braconnot, P., and Coauthors, 2007a: Results of PMIP2 coupled simulations of the mid-Holocene and Last Glacial Maximum—Part 1: Experiments and large-scale features. *Climate Past,* **3,** 261–277.

——, and Coauthors, 2007b: Results of PMIP2 coupled simulations of the mid-Holocene and Last Glacial Maximum—Part 2: Feedbacks with emphasis on the location of the ITCZ and mid- and high latitudes heat budget. *Climate Past,* **3,** 279–296.

Chiang, J., and C. Bitz, 2005: The influence of high latitude ice on the position of the marine intertropical convergence zone. *Climate Dyn.,* **25,** 477–496, doi:10.1007/s00382-005-0040-5.

Clement, A., and R. Seager, 1999: Climate and the tropical oceans. *J. Climate,* **12,** 3383–3401.

Czaja, A., and J. Marshall, 2006: The partitioning of poleward heat transport between the atmosphere and the ocean. *J. Atmos. Sci.,* **63,** 1498–1511.

Delworth, T. L., and Coauthors, 2006: GFDL'S CM2 global coupled climate models. Part I: Formulation and simulation characteristics. *J. Climate,* **19,** 643–674.

Dima, I., and J. Wallace, 2003: On the seasonality of the Hadley cell. *J. Climate,* **60,** 1522–1527.

Donohoe, A., 2011: Radiative and dynamic controls of global scale energy fluxes. Ph.D. thesis, University of Washington, 137 pp.

——, and D. Battisti, 2011: Atmospheric and surface contributions to planetary albedo. *J. Climate,* **24,** 4402–4418.

——, and ——, 2012: What determines meridional heat transport in climate models? *J. Climate,* **25,** 3832–3850.

——, and ——, 2013: The seasonal cycle of atmospheric heating and temperature. *J. Climate,* in press.

Eilers, P., and J. Goeman, 2004: Enhancing scatterplots with smoothed densities. *Bioinformatics,* **20,** 623–628.

Fasullo, J. T., and K. E. Trenberth, 2008: The annual cycle of the energy budget. Part II: Meridional structures and poleward transports. *J. Climate,* **21,** 2313–2325.

Frierson, D. M. W., and Y.-T. Hwang, 2012: Extratropical influence on ITCZ shifts in slab ocean simulations of global warming. *J. Climate,* **25,** 720–733.

Hadley, G., 1735: Concerning the cause of the general trade-winds. *Philos. Trans. Roy. Soc. London,* **29,** 58–62.

Haug, G., K. Hughen, D. Sigman, L. Peterson, and U. Röhl, 2001: Southward migration of the intertropical convergence zone through the Holocene. *Science,* **293,** 1304–1308.

Held, I., 2001: The partitioning of the poleward energy transport between the tropical ocean and atmosphere. *Science,* **58,** 943–948.

Kalnay, E., and Coauthors, 1996: The NCEP/NCAR 40-Year Reanalysis Project. *Bull. Amer. Meteor. Soc.,* **77,** 437–471.

Kang, S., I. Held, D. Frierson, and M. Zhao, 2008: The response of the ITCZ to extratropical thermal forcing: Idealized slab-ocean experiments with a GCM. *J. Climate,* **21,** 3521–3532.

Lin, S. J., 2004: A "vertically Lagrangian" finite-volume dynamical core for global models. *Mon. Wea. Rev.,* **132,** 2293–2307.

Lindzen, R., and A. Hou, 1988: Hadley circulations of zonally averaged heating centered off the equator. *J. Atmos. Sci.,* **45,** 2416–2427.

Meehl, G. A., C. Covey, T. Delworth, M. Latif, B. McAvaney, J. F. B. Mitchell, R. J. Stouffer, and K. E. Taylor, 2007: The WCRP CMIP3 multi-model dataset: A new era in climate change research. *Bull. Amer. Meteor. Soc.,* **88,** 1383–1394.

Pahnke, K., J. P. Sachs, L. Keigwin, A. Timmerman, and S. P. Xie, 2007: Eastern tropical Pacific hydrologic changes during the past 27,000 years from D/H ratios in alkenones. *Paleoceanography,* **22,** PA4214, doi:10.1029/2007PA001468.

Peltier, W., 2004: Global glacial isostasy and the surface of the ice-age earth: The ICE-5G (VM2) model and GRACE. *Annu. Rev. Earth Planet. Sci.,* **22,** 111–149.

Peterson, L., G. Haug, K. Hughen, and U. Röhl, 2000: Rapid changes in the hydrologic cycle of the tropical Atlantic during the last glacial. *Science,* **290,** 1947–1951.

Philander, S. G., D. Gu, D. Halpern, G. Lambert, N. Lau, T. Li, and R. Pacanowski, 1996: Why the ITCZ is mostly north of the equator. *J. Climate,* **9,** 2958–2972.

Reynolds, R., and T. Smith, 1994: Improved global sea surface temperature analyses. *J. Climate,* **7,** 929–948.

Sachs, J., D. Sachse, R. Smittenberg, Z. Zhang, D. Battisti, and S. Golubic, 2009: Southward movement of the Pacific inter-tropical convergence zone AD 1400–1850. *Nat. Geosci.,* **2,** 519–525.

Smith, T., R. Reynolds, T. Peterson, and J. Lawrimore, 2008: Improvements to NOAA's historical merged land–ocean surface temperature analysis (1880–2006). *J. Climate,* **21,** 2283–2296.

Takahashi, K., and D. Battisti, 2007: Processes controlling the mean tropical Pacific precipitation pattern. Part I: The Andes and the eastern Pacific ITCZ. *J. Climate,* **20,** 3434–3451.

Trenberth, K. E., 1997: Using atmospheric budgets as a constraint on surface fluxes. *J. Climate,* **10,** 2796–2809.

——, and J. M. Caron, 2001: Estimates of meridional atmosphere and ocean heat transports. *J. Climate,* **14,** 3433–3443.

Waliser, D., and C. Gautier, 1993: A satellite-derived climatology of the ITCZ. *J. Climate,* **6,** 2162–2174.

Wang, Y., H. Cheng, R. L. Edwards, Z. An, J. Wu, C.-C. Shen, and J. Dorale, 2001: A high-resolution absolute-dated late Pleistocene monsoon record from Hulu Cave, China. *Science,* **294,** 2345–2348.

Wielicki, B., B. Barkstrom, E. Harrison, R. Lee, G. Smith, and J. Cooper, 1996: Clouds and the Earth's Radiant Energy System (CERES): An earth observing system experiment. *Bull. Amer. Meteor. Soc.,* **77,** 853–868.

Xian, P., and R. Miller, 2008: Abrupt seasonal migration of the ITCZ into the summer hemisphere. *J. Atmos. Sci.,* **65,** 1878–1895.

Xie, P., and P. Arkin, 1996: Analyses of global monthly precipitation using gauge observations, satellite estimates, and numerical model predictions. *J. Climate,* **9,** 840–858.

Yoshimori, M., and A. J. Broccoli, 2008: Equilibrium response of an atmosphere mixed layer ocean model to different radiative forcing agents: Global and zonal mean response. *J. Climate,* **21,** 4399–4423.

——, and ——, 2009: On the link between Hadley circulation changes and radiative feedback processes. *Geophys. Res. Lett.,* **36,** L20703, doi:10.1029/2009GL040488.

Zelinka, M., and D. Hartmann, 2012: Climate feedbacks and their implications for poleward energy flux changes in a warming climate. *J. Climate,* **25,** 608–624.